JOURNAL OF GEOPHYSICAL RESEARCH, VOL. 104, NO. D13, PAGES 16,275–16,295, JULY 20, 1999

Use of a mixed-layer model to estimate dimethylsulfide flux and application to other trace gas fluxes

Donald H. Lenschow and Ilga R. Paluch

National Center for Atmospheric Research, Boulder, Colorado

Alan R. Bandy and Donald C. Thornton

Department of Chemistry, Drexel University, Philadelphia, Pennsylvania

Donald R. Blake and Isobel Simpson

Department of Chemistry, University of California, Irvine

Abstract. We discuss two techniques based on mixed-layer scaling for estimating trace gas surface emission fluxes from aircraft using instruments that do not have sufficient frequency response for direct eddy correlation measurements. The first is the mixed-layer gradient technique, which requires accurate measurements of mean concentrations at several heights in the clear convective planetary boundary layer (CBL) to resolve gradients from even strong surface sources of short-lived trace gases. The flux-gradient relationship is obtained from large-eddy numerical simulations of the CBL. We show that this technique is limited to trace gases with lifetimes of about a day or less. An example is dimethylsulfide (DMS), which is emitted from the ocean and has a lifetime of about a day. Surface DMS flux was estimated from data collected from the NASA P-3B research aircraft during the Pacific Exploratory Mission–Tropics (PEM-Tropics) flight 7 (August 24, 1996), when the aircraft flew a sequence of constant altitude circles about 50 km in diameter at different heights in and above the boundary layer, following the boundary layer air trajectory. The flight took place between 0530 and 1330 local solar time, providing a good opportunity to observe diurnal changes within a Lagrangian framework under nearly clear-sky conditions. The resulting DMS flux of 2.5 $\pm$ 0.8 pptv m s^{-1} (6.1 $\pm$ 1.9) $\times$ 10^{13} molecules m^{-2} s^{-1}, or 8.8$\pm$2.8 μmols m^{-2} d^{-1}) is on the high end of previous measurements in this milieu. The second technique is the mixed-layer variance technique, which uses measurements of the variance at several heights in the CBL to estimate the surface flux. A major problem with the variance technique is accounting for the contribution of mesoscale variability to the measured variance. Several sources of mesoscale variability were identified: clusters of small cumulus clouds rising through the top of the boundary layer, mesoscale variations in the horizontal wind leading to inaccurate tracking of the air mass and, to a lesser extent, the presence of horizontal roll vortices in some areas of the boundary layer. We show that the variance technique should be applicable to estimating surface fluxes of short-lived trace gases in cumulus-free boundary layers that are horizontally uniform, if sample-collection times of about 10 s or less are used. We also show that it may be possible to utilize mesoscale variance measurements to estimate surface fluxes and lifetimes of species which have lifetimes of perhaps a week or more.

1. Introduction

Dimethyl sulfide (DMS), produced by phytoplankton, is the dominant sulfur species emitted from the oceans [e.g., *Bates et al.*, 1992]. Its oxidation product, particulate sulfate, is believed to be the primary source of cloud condensation nuclei (CCN) in the remote marine atmosphere. The potential link between DMS and CCN in the marine troposphere was postulated by *Charlson et al.* [1987] as a possible negative feedback for control of global warming. This hypothesis has generated much interest in the measurement of DMS.

Paper number 1998JD100090.
0148-0227/99/1998JD100090$09.00

However, due to low concentrations (≤300 pptv) and irreversible adsorption of DMS in many analytical systems, the measurement of atmospheric DMS has been restricted to grab sampling techniques [*Andreae and Andreae*, 1988; *Bates et al.*, 1990; *Eisele and Berresheim*, 1992; *Berresheim et al.*, 1993]. Typically, DMS is measured via sampling onto sorbents or cryogenically, then analyzed via gas chromatography with flame photometric, mass spectrometric, or electron capture detection [*Bandy et al.*, 1992, 1993; *Berresheim et al.*, 1993; *Blomquist et al.*, 1996]. Loss of temporal resolution due to slow sampling (~5-15 min) and analysis time (~5-30 min) preclude the use of direct eddy correlation or variance techniques.

In the Pacific Exploratory Mission–Tropics (PEM-Tropics), DMS was sampled over 5 min intervals, which corresponds to a distance of about 30 km. Therefore we resort to estimating fluxes by using a mixed-layer model that relates fluxes at the surface and the top of the clear convective boundary layer (CBL) to the gradient in concentration throughout the CBL. *Russell et al.* [1998] have used the same technique for estimating DMS emission during the first Aerosol Characterization Experiment (ACE 1).

In addition to DMS, which has a lifetime of about a day, other photochemically reactive species with sources at the surface, but with lifetimes of 4 to 25 days, were measured in PEM-Tropics: bromoform ($CHBr_3$), methyl iodide (CH_3I), methyl nitrate (CH_3ONO_2), and ethyl nitrate ($C_2H_5ONO_2$). These species were measured from grab samples collected over a period of about 1 min every 5 min. We show that 1 min (6 km) is too long a collection time for estimating surface flux by variance that scales with the height of the boundary layer z_i, which here was 570 m. Furthermore, 4 days may already be too long to obtain estimates of their lifetimes and surface fluxes from mixed-layer scaling with the PEM-Tropics data. Yet we observe significant variance in these species which give unreasonably short lifetimes if mixed-layer variance scaling is applied. We show that this is likely due to mesoscale variability, which is linked to surface flux and to the species lifetime through entrainment processes. Thus we hypothesize that estimates of surface flux and species lifetimes can be obtained from mixed-layer variance on the mesoscale.

2. Flux Measurement by Mixed-Layer Scaling Techniques

2.1. Mixed-Layer Gradient Technique

The top-down/bottom-up (TD-BU) mixed-layer gradient technique was first proposed by *Wyngaard and Brost* [1984]. The technique relates mixed layer gradients and variances of scalars to fluxes at the surface (surface emission or deposition) and at the top of the CBL (entrainment). *Moeng and Wyngaard* [1984, 1989] further refined the formulations using large-eddy numerical simulations (LES) of the CBL. The first applications of this to flux measurements as well as limitations and conditions under which the TD-BU technique can be used were reported by *Davis* [1992] and *Davis et al.* [1994]. They obtained flux measurements of nonmethane hydrocarbons from tethered balloon profiles in the Amazon and southeastern United States and also applied the technique to aircraft measurements to show that the LES-derived gradient functions were consistent with observations. The TD-BU technique is based on two hypotheses. The first is the concept of mixed-layer similarity. The mixed layer is that part of the CBL lying above the surface layer (typically the first few tens of meters above the surface where the fluxes can be considered constant) and below the turbulent entrainment layer that caps the CBL. The hypothesis argues that by scaling the mixed layer with z_i, the convective velocity scale,

$$w_* \equiv \left(\frac{g}{T} F_0 z_i\right)^{1/3}, \tag{1}$$

and surface and entrainment fluxes of scalars, we can obtain universal formulations for mean and turbulence variables as functions of normalized height $z_* = z/z_i$. In (1), g is the acceleration of gravity, T is temperature, and F_0 is the virtual temperature flux at the surface. The second hypothesis is that the transport of scalars from the top of the CBL down and from the bottom up are independent and each obeys a separate flux-gradient relationship. That is,

$$\frac{\partial S}{\partial z} = -g_b(z_*)\frac{F_{s_0}}{z_i w_*} - g_t(z_*)\frac{F_{st}}{z_i w_*}, \tag{2}$$

where $g_b(z_*)$ and $g_t(z_*)$ are the dimensionless bottom-up and top-down scalar gradient functions, and F_{s_0} and F_{st} are the surface and entrainment fluxes, respectively, of a scalar S.

The measurements available from field studies are concentration differences rather than gradients. Therefore, to estimate fluxes, (2) must be integrated between two levels z_{*1} and z_{*2},

$$S_2 - S_1 = -\frac{F_{s_0}}{w_*}\int_{z_{*1}}^{z_{*2}} g_b(z_*)dz_* - \frac{F_{st}}{w_*}\int_{z_{*1}}^{z_{*2}} g_t(z_*)dz_*. \tag{3}$$

Since the right side of (3) contains two unknowns, F_{s0} and F_{st}, a minimum of three flight levels are required in order to estimate two differences.

Figure 1 shows the TD-BU gradient functions $g_t(z_*)$ and $g_b(z_*)$ for a buoyancy-driven CBL [*Moeng and Wyngaard*, 1984, 1989]. Various piecewise approximations have been used for integrating these functions. Here we integrate them directly from tabulated values (C.-H. Moeng, personal communication, 1998).

The TD-BU gradient relationships have been derived for conserved scalars. These relationships should also hold for nonconserved scalars whose characteristic diurnally averaged growth or decay time,

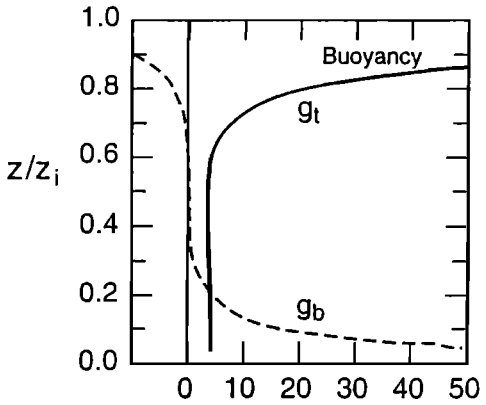

Figure 1. The dimensionless top-down and bottom-up gradient functions $g_t(z_*)$ and $g_b(z_*)$ from large-eddy simulations of a buoyancy-driven turbulent boundary layer.

$$\tau_s \equiv [(1/S)D_s]^{-1}, \quad (4)$$

is much slower than the characteristic turbulent mixing time [*Lenschow*, 1995],

$$\tau_t \equiv z_i/w_*. \quad (5)$$

Here D_s is the diurnally averaged chemical rate of production or destruction of S (roughly 1/3 the midday growth/decay rate for photochemically reactive species). For flight 7, $z_i = 570$ m, $w_* = 0.58$ m s^{-1}, and thus $\tau_t = 17$ min. This is far shorter than the growth and decay times of the trace gases considered here, whose lifetimes are given in Table 1.

2.2. Mixed-Layer Variance Technique

Employing the TD-BU formulation, *Moeng and Wyngaard* [1984, 1989] also found from the LES results that the variance profile of a trace species generated by surface and entrainment fluxes that scale with z_* is given by

$$\sigma_s^2(z_*) = \left(\frac{F_{s0}}{w_*}\right)^2 f_b + 2\left(\frac{F_{s0}F_{st}}{w_*^2}\right) f_{bt} + \left(\frac{F_{st}}{w_*}\right)^2 f_t, \quad (6)$$

where $f_b \simeq z_*^{-0.9}$, $f_t \simeq 3.1(1 - z_*)^{-3/2}$, and $f_{bt} \simeq 1.5$ are the dimensionless bottom-up and top-down variance functions, and the TD-BU covariance function, respectively. For better accuracy, the values of the above functions can be read directly off the plots of LES results given by *Moeng and Wyngaard* [1989]. If the variances at any two levels of the sounding are known, then (6) can be solved for F_{s_0} and F_{st} by successive approximations or graphical methods.

The variance technique could be useful for evaluating fluxes for trace species whose gradients are too weak to be measured accurately and if the sampling time or sensor time constant is too long for a direct eddy-correlation approach, but short enough to resolve a significant fraction of the variance at the long-wavelength end of the power spectrum. The partial variance may then be related to the total variance by a scaling factor. If we can assume spectral similarity, then this scaling factor could be obtained from a reference scalar for which high-rate data are available. Using this approach, the variance technique could be applied to flask samples, if the sample collection time is short enough, and a sufficient number of samples is collected.

At first glance, it may seem that the variance technique is inherently more accurate than the gradient technique since variances can often be measured more accurately than mean differences and, disregarding other sources of error, the accuracy in the flux estimate is approximately equal to the accuracy in the variance estimate. However, a major problem is the difficulty in estimating the impact of mesoscale processes, as well as heterogeneity in the surface and CBL top on the production of variance.

3. Measurements

The data analyzed here were collected from the NASA P-3B research aircraft during PEM-Tropics flight 7. *Davis et al.* [this issue] and *Considine et al.* [this issue] give more details on the general conditions for this flight. On this day the aircraft flew constant altitude circles about 50 km in diameter (30 min duration) at different heights in the CBL in the vicinity of Christmas Island (2°N, 157.5°E). The sequence of circles approximately follows the air mass trajectory in the CBL, which traveled to the WNW. The portion of the flight track within the CBL is plotted in Figure 2.

In addition to the standard meteorological measurements (air and dew point temperatures, static pressure, etc.) recorded at 1 s intervals (or 100 m spacing for a typical P-3B airspeed of 100 m s^{-1}, the Turbulent Air

Table 1. Estimated Diurnally Averaged Lifetime of Photochemically Active Trace Species at the Equator Using Measured OH Concentrations, and Measured Normalized Standard Deviations and Mean Concentrations Measured With the NASA P-3B on Flight 7

Species	Lifetime Days	$\frac{\sigma_s}{S}$	S, pptv
DMS	1	n/a	n/a
CH_3I	4	0.047	0.497
$CHBr_3$	13	0.054	2.235
CH_3ONO_2	26	0.045	31.64
$C_2H_5ONO_2$	11	0.047	11.305
CFC-12	∞	0.0086	521.4

The standard deviation represents fluctuations collected from five or six samples over the flight leg with a sample collection time of 1 min (or 6 km distance, which is $10z_i$). The variances σ_s^2 were calculated after removing the diurnal variability, then normalized by the mean concentration at that level S.

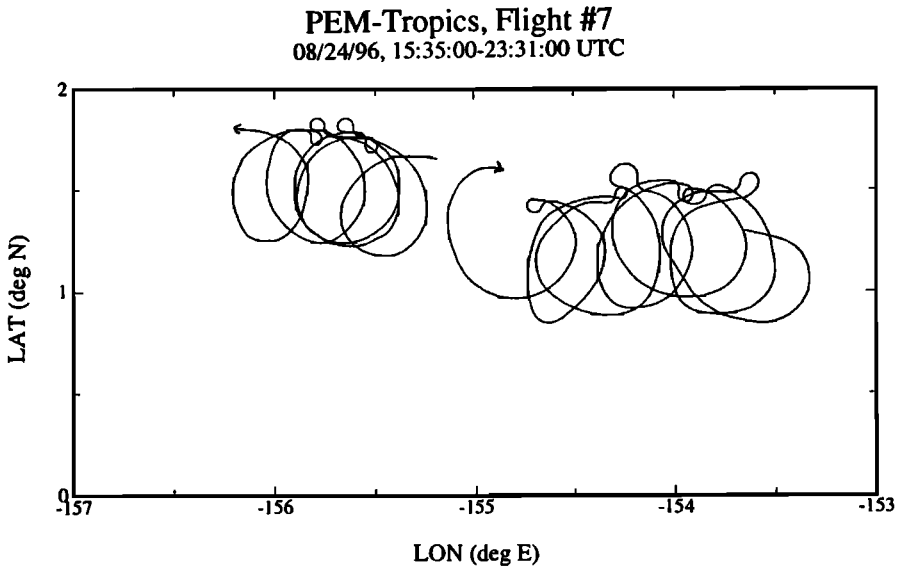

Figure 2. A partial view of the flight track on flight 7 (August 24, 1996, 1535–2331 UTC). The local solar time is 10 hours before UTC. To avoid clutter, the flight track from soundings is not included. The positions of the circles approximately follow the WNW air mass trajectory in the boundary layer.

Motion Measurement System (TAMMS) recorded high-rate velocity, temperature, and humidity data at about 18 samples s^{-1}. The high-rate humidity data were obtained from a Lyman-alpha hygrometer. Because its calibration tends to drift with time, the data were normalized using a slower responding GE 1011 dew/frost point hygrometer. (The high-rate humidity data were recorded in units of g m^{-3} (J. Barrick, personal comunication, 1998), but the fluxes and variances here are converted to g kg^{-1}.) In the CBL on flight 7 the fast-response temperature probe frequently shorted out due to contamination by salt particles; thus the data were not suitable for flux and variance calculations in the CBL.

DMS and SO_2 were sampled over 5 min (30 km) intervals, whereas most other trace gas species concentrations considered here were estimated from grab samples collected over a 1 min (6 km) period roughly once every 5 min [*Bandy et al.*, 1993; *Blake et al.* 1996].

4. Diurnal Variations

On flight 7 the CBL data were collected between 0530 and 1330 local solar time, during which the concentrations of DMS, SO_2, $CHBr_3$, and CH_3I underwent gradual changes, as shown in Figures 3 and 4. The squares, crosses, and asterisks mark data from circles in the boundary layer where $z_* = 0.11, 0.27$, and 0.53, respectively. The low DMS and SO_2 concentrations represent data collected above the CBL. The DMS destruction and the SO_2 production rates nearly balance each other, producing little change in the total DMS + SO_2 concentration. The estimated net rates, represented by the slopes of the lines in Figures 3 and 4, are listed in Table 2. During the flight the sky was mostly clear, with some small scattered clouds above the CBL (see Figure 10).

To obtain changes in concentration as a function of z_*, all CBL data were normalized to the early morning values. Vertical gradients in DMS, SO_2, $CHBr_3$, CH_3I, CH_3ONO_2, and $C_2H_5ONO_2$ are shown in Figure 5. The error bars represent the 90% confidence limit using the Student's t test. As can be seen, the expected errors tend to be large. They arise from horizontal variability coupled with limited sampling intervals. We shall limit surface flux calculations to DMS because only DMS shows a significant gradient near the surface that is well outside the range of the error bars.

5. DMS Surface Flux Estimates

5.1. Flux From Mixed-Layer Gradients

In this section we carry out the evaluation of DMS emission from the ocean. To do this, we first need to evaluate the convective velocity w_*. Since we were not able to estimate the surface buoyancy flux directly, we estimate w_* by the following two techniques: (1) using the relation for the vertical velocity variance in the mixed layer [*Lenschow et al.*, 1980],

$$\sigma_w^2(z_*) = 1.8{z_*}^{2/3}(1. - 0.8z_*)^2{w_*}^2. \qquad (7)$$

From soundings, we estimate z_i = 570 m. For flight levels z_* = 0.11, 0.27, and 0.53, which we denote as levels 1 to 3, we obtain σ_w = 0.34, 0.39, and 0.35 m s^{-1}, which give w_* = 0.58, 0.58, and 0.56 m s^{-1}. This

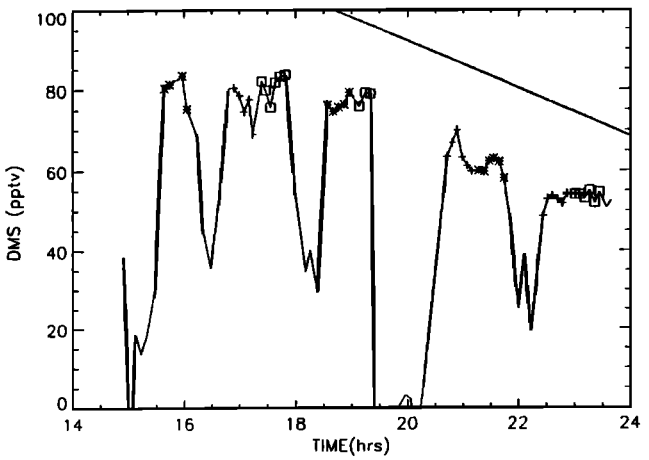

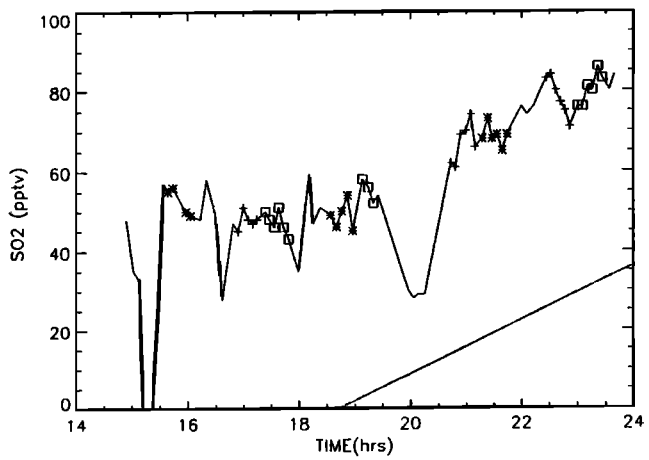

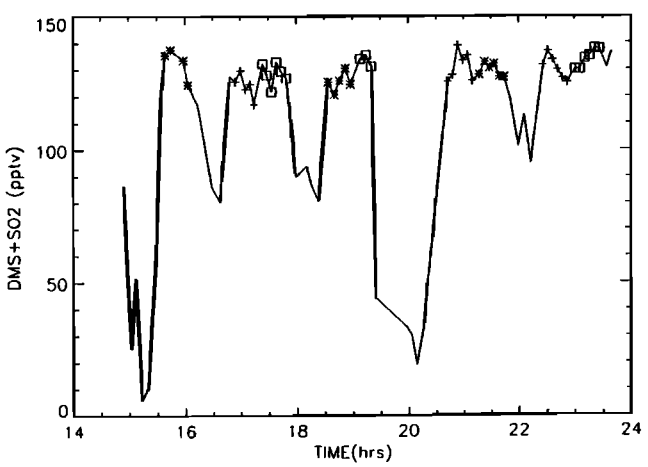

Figure 3. Changes in DMS and SO_2 concentrations with time (UTC). The local solar time is 10 hours earlier. The squares, crosses, and asterisks represent 5 min data samples from circles in the boundary layer where the normalized altitude z_* is 0.11, 0.27, and 0.53, respectively. Lower DMS and SO_2 concentrations were observed above the boundary layer. To avoid clutter, these samples are not marked by symbols. The straight line shows the diurnal changes in DMS and SO_2, estimated so as to minimize variance in the normalized data set.

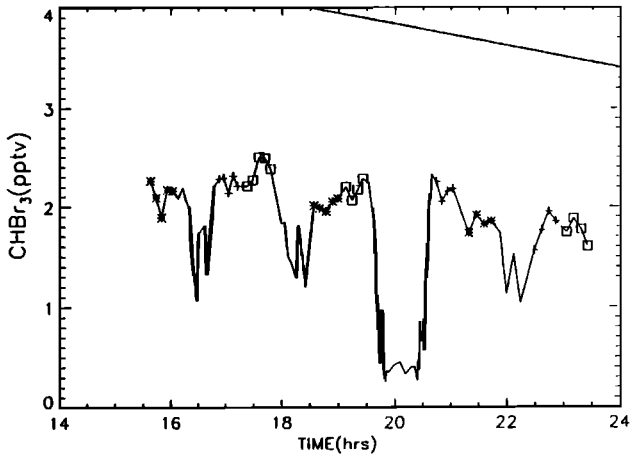

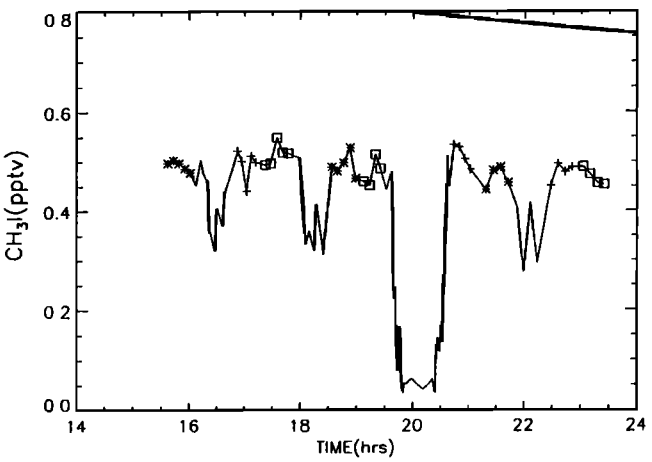

Figure 4. Same as Figure 3, but for $CHBr_3$ and CH_3I.

agrees well with the estimates of *Considine et al.* [this issue]. (2) Using the aerodynamic transfer technique [e.g., Lenschow, 1995] to estimate the surface temperature and humidity fluxes is the other means for estimating w_*. We assume a transfer coefficient for both of 1.3×10^{-3}, use the measured radiation sea surface temperature of 26.8°C, and estimates of the air temperature and humidity at the reference height for the aerodynamic transfer calculation of 299.1 K and 16.5 g kg^{-1}, respectively, to obtain $w_* = 0.72$ m s^{-1}. However, primarily because of possible errors in the air and sea surface temperatures (J. Barrick, personal communica-

Table 2. Estimates of time changes in species concentration measured from the NASA P-3B during Flight 7

Species	t_0, hours. solar time	$\frac{ds}{dt}$, pptv h^{-1}	$\frac{1}{S}\frac{ds}{dt}$, h^{-1}
DMS	8.75	-6.0	-0.10
SO_2	8.75	7.0	0.12
$CHBr_3$	8.50	-0.12	-0.06
CH_3I	10.0	-0.012	-0.025

Here t_0 is the starting time for the estimates.

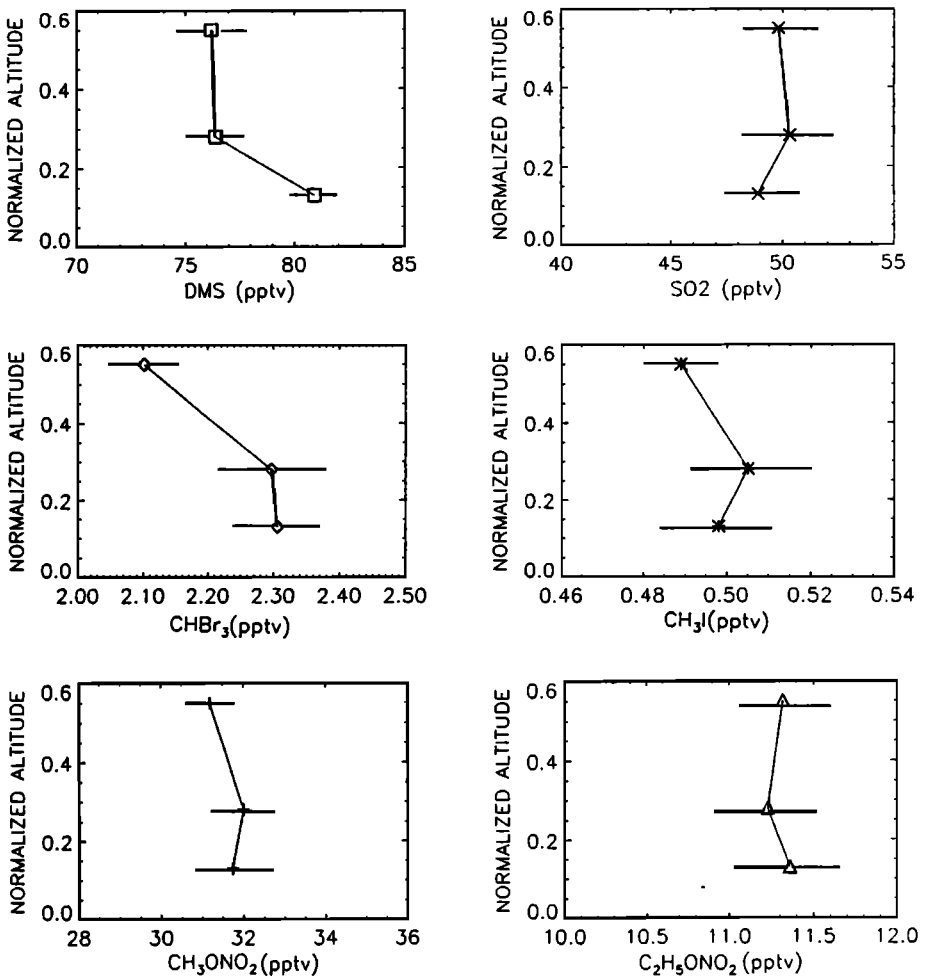

Figure 5. Vertical profiles of DMS, SO_2, $CHBr_3$, CH_3I, CH_3ONO_2, and $C_2H_5ONO_2$ as a function of normalized altitude z_*. The error bars represent the 90% confidence limit using the Student's t test.

tion, 1998), we consider technique 2 to be less accurate than technique 1 and use $w_* = 0.58$ m s^{-1}.

The measured concentration differences inserted into (3) are $S_2 - S_1 = 4.5 \pm 1.8$ parts per trillion by volume (pptv) and $S_3 - S_1 = 4.7 \pm 1.8$ pptv, where the plus or minus values are the 90% confidence limits for the Student's t test. Solving the above equations gives a small negative (downward) DMS flux at the CBL top ($F_{st} = -0.3 \pm 1.3$ pptv m s^{-1}), which is insignificantly different from zero, and physically implausible, since the DMS concentration drops rapidly above the CBL top (Figure 3). Hence we calculate the DMS surface flux assuming that the DMS flux at the CBL top is zero. (Ignoring the negative F_{st} has a negligible effect on the surface flux estimate.) For the lowest two flight levels this gives $F_{s0} = 2.6 \pm 1.0$ pptv m s^{-1} ($6.3 \pm 2.4 \times 10^{13}$ molecules m^{-2} s^{-1}, or 9.1 ± 3.5 μmols m^{-2} d^{-1}). As before, the estimated errors represent the 90% confidence limit in the Student's t test. Similarly, for flight levels 1 and 3: $F_0 = 2.4 \pm 0.9$ pptv m s^{-1} ($5.9 \pm 2.2 \times 10^{13}$ molecules m^{-2} s^{-1}, or 8.5 ± 3.2 μmols m^{-2} d^{-1}). Thus the average flux of DMS is 2.5 ± 0.8 ppt m s^{-1} ($6.1 \pm 1.9 \times 10^{13}$ molecules m^{-2} s^{-1}).

5.2. Comparisons With Previous DMS Flux Estimates

Davis et al. [this issue] used the measured mean DMS concentrations from flight 7 in a mass conservation model that included photochemical reactions and parameterized transport terms to estimate a surface flux of $F_0 = 1.0 \pm 0.6$ pptv m s^{-1} ($2.3 \pm 1.4 \times 10^{13}$ molecules m^{-2} s^{-1}). We can also compare our results with the estimates from *Bandy et al.* [1996], who report $F_0 = 1.5$ pptv m s^{-1} (3.7×10^{13} molecules m^{-2} s^{-1} or 5.3 μ mols m^{-2} d^{-1}) for the average surface DMS flux deduced from mean DMS measurements on the northeast end of Christmas Island at the top of a 20 m tower, 15 m from the ocean, during July and August 1994. The flux estimate was based on nighttime observations and column budgets (no advection of horizontal inhomogeneities), assuming an entrainment velocity at the CBL top of 5 mm s^{-1}. The surface DMS flux estimates for 5 different days ranged from 0.9 to 1.8 pptv ms^{-1} (2.2 to 4.5×10^{13} molecules m^{-2} s^{-1} or (3.2 to 6.5 μmols m^{-2} d^{-1}). In the Soviet-American Gas and Aerosol Experiment (SAGA 3) in the equatorial Pacific, *Bates et*

al. [1993] used DMS partial pressures in surface seawater and the overlying atmosphere, and wind speed measured aboard a ship, to derive an average DMS surface flux of 7.1 μmols m^{-2} d^{-1} (4.9×10^{13} molecules m^{-2} s^{-1}, or 2.0 pptv m s^{-1}), with maximum values reaching 21.2 μmols m^{-2} d^{-1} (14.7×10^{13} molecules m^{-2} s^{-1}, or 6.0 pptv m s^{-1}).

Compared to the other estimates of DMS surface flux, our average value of 2.5 ± 0.8 pptv m s^{-1} for flight 7 is on the high side, but in view of the variability of the observed fluxes, it is not inconsistent with previous measurements.

During the daytime on flight 7 the DMS concentration in the CBL decreased at a rate of about 6 pptv h^{-1} (144 pptv d^{-1}). This is at the low end of the *Bandy et al.* [1996] observations which for daytime hours are in the range of 143–393 pptv d^{-1}.

Assuming no diurnal variations in the surface flux, the expected increase in DMS in the CBL due to surface flux alone would be (2.5 pptv m $s^{-1}\times$ 3600 s h^{-1})/570 m = 16 pptv h^{-1} (380 pptv d^{-1}). This value is significantly higher than the 95–216 pptv d^{-1} increase that *Bandy et al.* [1996] estimated for nighttime conditions, who also estimated a DMS flux through the CBL top of 53–98 pptv d^{-1}.

On the basis of the data presented here, the upper limit for the daytime DMS chemical destruction rate (i.e., the rate at which DMS is being destroyed rather than the observed rate of concentration decrease), assuming zero flux at the boundary layer top, is 22 pptv h^{-1} (530 pptv d^{-1}), whereas *Bandy et al.'s* [1996] data are in the 332–505 pptv d^{-1} range. (These rates pertain to midday hours; the diurnally averaged rates are about 1/3 of the above values.)

6. Applications and Limitations of the Mixed-Layer Gradient Approach

The mixed-layer gradient approach works well for species with a lifetime of order 1 day such as DMS. However, as we show here, it is not applicable to species with lifetimes much greater than a day. To demonstrate this, we start with the budget equation for a reactive trace species in a horizontally homogeneous CBL:

$$\frac{dS}{dt} = -\frac{\partial F_s}{\partial z} - W\frac{\partial S}{\partial z} - D_s, \tag{8}$$

where the mean vertical air velocity is related to the mean atmospheric subsidence sub(z) by the relation

$$W(z) = -\int_0^z \mathrm{sub}(z')dz'. \tag{9}$$

We average a photochemically reactive species across the diurnal cycle and assume the diurnally averaged concentration is in steady state. Then integrating (8) across the CBL where $\partial S/\partial z$ is small, and introducing (4) gives

$$F_{s0} - F_{st} = \int_0^{z_i} D_s dz \equiv \frac{\langle S\rangle}{\tau_s} z_i, \tag{10}$$

where $\langle S\rangle$ is an average concentration through the entire CBL.

The error bars in Figure 5 place limits on the minimum gradients that can be measured near the surface. To estimate this minimum gradient, we assume negligible entrainment flux so that (10) reduces to

$$F_{s0} \simeq \langle S\rangle \frac{z_i}{\tau_s}. \tag{11}$$

Therefore, with (4), (5), and (11), the relationship (3) can be expressed as

$$(S_1 - S_2)/\langle S\rangle \simeq (\tau_t/\tau_s)\int_{z_{*1}}^{z_{*2}} g_b(z_*)dz_*. \tag{12}$$

For the present case, τ_t = 17 min, and the integral of the bottom-up gradient function $g_b(z_*)$ between z_* = 0.11 and 0.53 is 1.14. For gases other than DMS the error bars in Figure 5 are at about ±3%, which when substituted for $(S_1 - S_2)/\langle S\rangle$ gives τ_s = 10 hours. Thus, for the flight altitudes, sampling strategy, and meteorological and chemical environment that characterize flight 7, we would not expect to see surface gradients for gases whose lifetimes are much longer than 10 hours. (The 10 hours is conservative, since this assumes that the measurements in each flight circle are independent.) The lifetime for CH_3I is about 4 days, and for $CHBr_3$, CH_3ONO_2, and $C_2H_5ONO_2$ it is about 1–2 weeks, which explains why the mixed-layer gradients for these gases (shown in Figure 5) are not well-defined, although both CH_3I and $CHBr_3$ show a significant decrease at the upper level compared to the two lower levels. These are the two species (besides DMS and SO_2) that also show a significant diurnal change. Their daytime decay rates (Table 2) indicate a diurnally averaged lifetime of 5 days for CH_3I and 2 days for $CHBr_3$, in contrast to the values predicted in Table 1 of about 4 and 13 days, respectively.

The τ_s estimate is quite sensitive to the lowest measured value of z_*, since $g_b(z_*)$ increases rapidly as $z_* \to 0$ (Figure 1). For example, if the flight level were lower or the CBL top were higher so that the lowest z_* = 0.07, instead of 0.11, then the integrated value of $g_b(z_*)$, and consequently the maximum value of τ_s that can be estimated, would be about 2 times larger.

We can extend our consideration of the concentration profile to levels above the CBL, since profiles even for species with lifetimes of the order of a day (e.g., DMS) indicate significant concentrations above the CBL. As discussed, for example, by *Russell et al.* [1998], entrainment can occur in both directions across the CBL top, due to both cloud and clear-air processes. In the presence of clouds this layer immediately above the CBL, which contains a mixture of CBL and free-tropospheric air, has been called the cloud layer [e.g., *LeMone*, 1980]. However, since this two-layer structure can also form in

the absence of clouds, following Russell et al., we call this layer the buffer layer (BuL). Integrating (8) from z_i to a level h_s where $S \to 0$,

$$F_{st} = \int_{z_i}^{h_s} \left(D_s + W \frac{\partial S}{\partial z} \right) dz. \tag{13}$$

Therefore, substituting (13) into (10),

$$F_{s0} = \frac{\langle S \rangle z_i}{\tau_s} + \int_{z_i}^{h_s} \left(\frac{S}{\tau_s} + W \frac{\partial S}{\partial z} \right) dz. \tag{14}$$

Equation (14) can also be used to estimate the surface flux for a steady state species (averaged over the diurnal cycle) whose sole source is at the surface and whose destruction rate is proportional to the mean concentration without assuming negligible transport across the CBL top. The ratio of the second (mean motion) term to the first term in the integral term of (14) is $\bar{W}\tau_s/H$, where $\bar{W}$ is a characteristic mean vertical velocity of the layer over which we integrate, typically of order 10^{-3} m s^{-1} in the tropical CBL [*Fuelberg et al.*, this issue], and H is an equivalent height defined by

$$H = \langle S \rangle^{-1} \int_{z_i}^{h_s} S dz. \tag{15}$$

A typical value for H over the tropical ocean is of order 10^3 m. Thus the contribution of the second term in the integral term of (14) is only significant (on about the 10% level) if τ_s is greater than about a day (and thus typically is marginally significant for DMS). If τ_s is less than about a day,

$$\tau_s F_{s0} = \langle S \rangle z_i + \int_{z_i}^{h_s} S dz, \tag{16}$$

so that knowing the mean concentration profile and either the surface flux or the time constant, we can solve for the remaining unknown. Equation (16) (or (14) for cases when the mean motion term is significant) should be useful for species with considerably longer lifetimes than those for which (12) can be used.

Finally, we note that we can estimate the ratio of species lifetimes through the following approach. From (4) and (13), assuming negligible mean vertical velocity, we have

$$F_{st} = \tau_s^{-1} \int_{z_i}^{h_s} S dz. \tag{17}$$

As shown by *Russell et al.* [1998], we can also write

$$F_{st} = -w_{eb} \Delta S, \tag{18}$$

where w_{eb} is the entrainment velocity of air from the CBL into the BuL and $\Delta S = S_{Bu} - \langle S \rangle$ is a characteristic jump in S across the CBL top. We can combine (17) and (18), carry out the same procedure for another species R with a different reaction time τ_r, and take the ratio of the two to obtain

$$\frac{\tau_s}{\tau_r} = \frac{\Delta R \int_{z_i}^{h_s} S dz}{\Delta S \int_{z_i}^{h_r} R dz}. \tag{19}$$

As pointed out by *Lenschow* [1996], estimating the appropriate jump in species concentration to use in (18) is difficult, especially when the jump is small (as is the case for longer-lived species). However, taking the ratio of the two species means that we need only select the same measurement levels for both species to estimate the jump.

We can test the timescale ratio relationship (19) for DMS and CH_3I using the observed vertical profiles given by *Davis et al.* [this issue]. We find that selecting the upper level at ~900 m, where a set of DMS measurements were obtained, the observations indicate a timescale ratio of CH_3I to DMS of about 5, which is in reasonable agreement with the predicted ratio (Table 1).

7. Variance Technique

In this section we discuss the mixed-layer variance technique for variance generated by surface and entrainment fluxes that scale with z_i, as has been studied by LES. The observations show, however, that variance exists at horizontal scales longer than z_i.

7.1. Scale-Dependent Contributions to Moisture Flux and Variance

During PEM-Tropics a number of trace species were averaged over a 1 min (6 km) sampling period, which for the present CBL correspond to a horizontal distance of $10z_i$. The variance technique, on the other hand, depends on variance functions obtained via an LES model covering a $5z_i$ by $5z_i$ area [*Moeng and Wyngaard*, 1984]. Thus the current variance formulation applies only to fluxes and variances up to $5z_i$ wavelengths. One approach we considered was to extend the variance technique to longer wavelengths by using a surrogate scalar with a large surface flux for which smaller-scale measurements were available. Here humidity was used, since it was sampled at about 18 s^{-1} by the TAMMS. We can then try to calculate a scale factor that relates contributions to the humidity variance for wavelengths $>10z_i$ to contributions for wavelengths $<5z_i$.

Figure 6 shows the power spectra of humidity and vertical velocity fluctuations, and their cospectra for a 50 km ($88z_i$) diameter circle at $z_* = 0.11$. Here the longer wavelengths (i.e., >5 km) make significant contributions to the humidity variance (area under the power spectrum) but contribute very little to the vertical velocity variance and, consequently, little to the total humidity flux F_q (area under the cospectrum). Here, and in other data not shown, the contribution from wavelengths $>10z_i$ to the total humidity flux is quite variable, so that no well-defined relationship can be established between humidity variance contributions for wavelengths $>10z_i$ and wavelengths $<5z_i$.

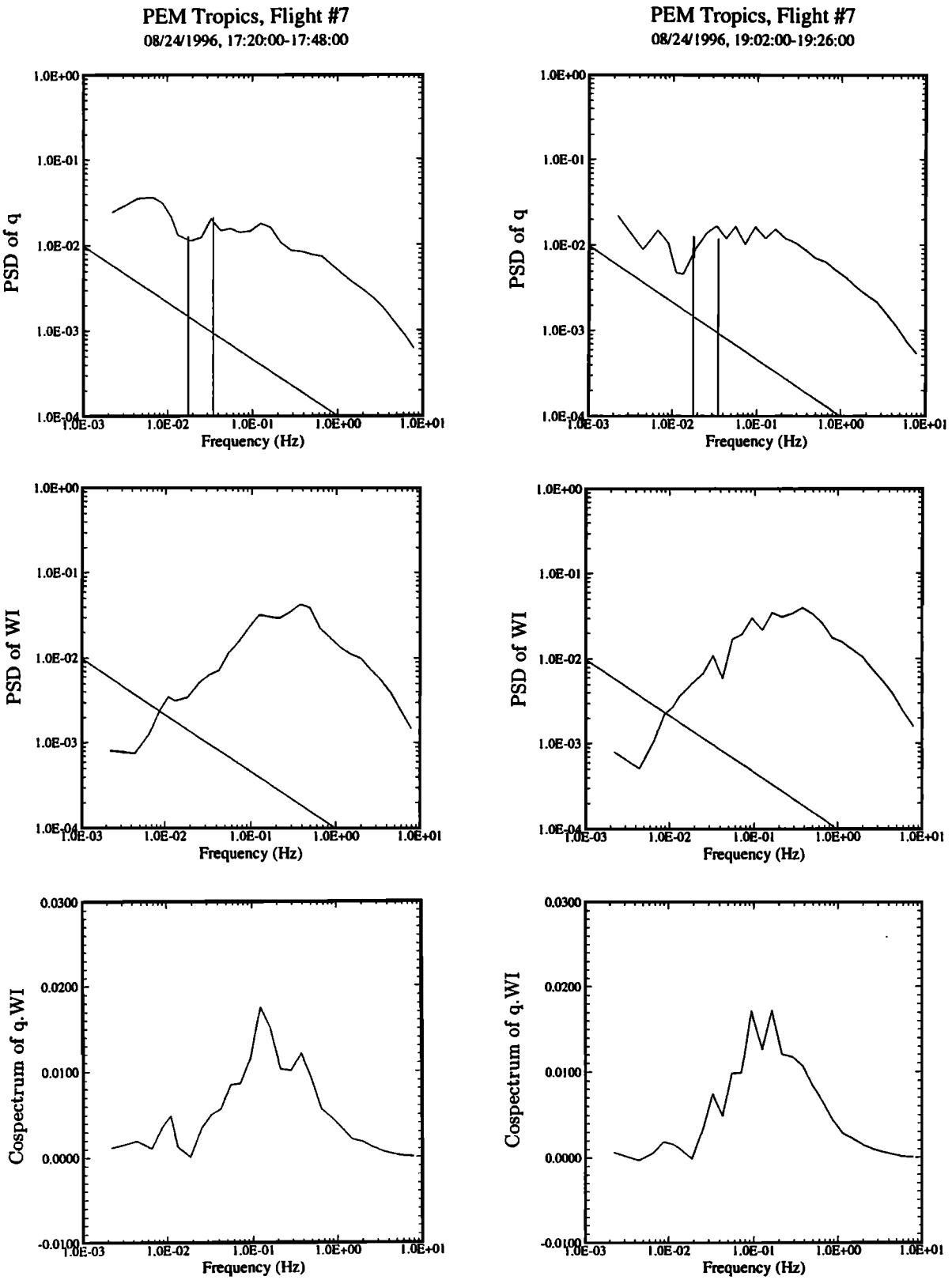

Figure 6. Mesoscale contributions to power spectra (PSD) times frequency of specific humidity (q, $g^2\ kg^{-2}$), vertical velocity (WI, $m^2\ s^{-2}$), and their cospectra. The plots are based on high-rate data, collected at about 18 samples/s, during the first two circles at $z_* = 0.11$. The diagonal line in the power spectra plots shows the 2/3 slope, characteristic of turbulence in the inertial subrange. The two vertical lines on the q power spectra mark frequencies at $10z_i$ and $5z_i$.

We conclude therefore that the 1 min ($10z_i$) averaging time for trace gas species is clearly too long to obtain a reliable scaling factor from the present high-rate humidity data to estimate surface flux from variance generated by eddies that scale with z_i. However, if the sampling time were reduced to 10 s, which is probably the shortest feasible sampling time for flask samples, then the samples would average over wavelengths up to 1 km, which here corresponds to $1.8z_i$. This cutoff would allow measurement of variance at scales that include contributions by eddies that scale with the convective eddies driven by the surface buoyancy flux, so that there would be a much better chance for obtaining a reliable scaling factor relating the variance scaling with z_i to the flux.

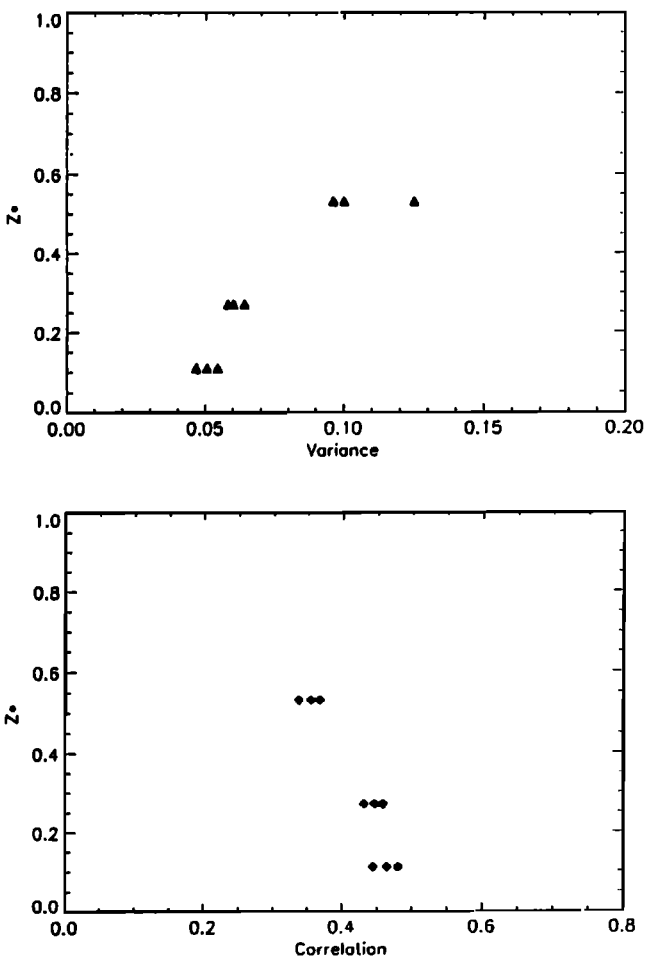

Figure 7. The humidity variance $(\sigma_q)^2$ (g kg^{-1})^2 and the correlation coefficient $F_q/(\sigma_w\sigma_q)$ for wavelengths $< 5.3z_i$. Each data point represents the variance calculated from high-rate data during one constant-altitude circle. The data were collected from 0530 to 1330 local time (1536–2330 UTC). The highest variance value (0.125 at $z_* = 0.53$) comes from the first circle 0536–0602 local time.

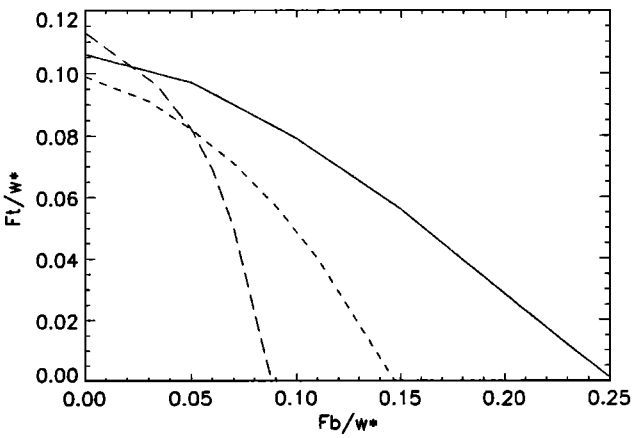

Figure 8. Normalized top-down and bottom-up fluxes (F_t/w_* and F_b/w_* in g kg^{-1}) calculated from (6) using measured variances for wavelengths $< 5.3z_i$. The long-dashed, short-dashed, and solid lines represent altitudes $z_* = 0.11, 0.27$, and 0.53, respectively. Ideally, the curves should cross at one point, thus giving unique values for F_t/w_* and F_b/w_*, but here this is not the case. For comparison, the direct eddy correlation technique gives $F_b/w_* = 0.06$ g kg^{-1}.

7.2. Applying the Variance Technique to the Short-Wavelength End of the Spectrum

When contributions at wavelengths longer than about $5z_i$ are excluded, the humidity fluxes and variances show consistent relationships from one circle to the next at a given altitude within the CBL, in agreement with the results of *Mann and Lenschow* [1994]. Figure 7 shows the humidity variance σ_q^2 and the correlation coefficient $F_q/(\sigma_w\sigma_q)$ at different altitudes and times, where σ_w is the vertical velocity standard deviation. (We have used a cutoff wavelength of $5.3z_i$ instead of $5z_i$ for computational convenience.) The correlation coefficient here remains nearly constant, while the humidity variance and flux decrease somewhat with time. This suggests that it may be possible to apply the variance technique to the high-rate humidity fluctuations at the short wavelength end of the spectrum.

Averaged over three constant altitude circles at $z_* = 0.11$, 0.27, and 0.53, the humidity variances for wavelengths $<5.3z_i$ are 0.050, 0.061, and 0.107 (g/kg)^2 respectively. Figure 8 shows the relationship between normalized TD-BU humidity fluxes (F_{qt}/w_* and F_{q0}/w_*) calculated from (6) using the above humidity variances together with variance functions from *Moeng and Wyngaard* [1989]. For $z_* = 0.11$ and 0.27, the curves intersect at about $F_{qt}/w_* = 0.08$ g kg^{-1} and $F_{q0}/w_* = 0.05$ g kg^{-1}. The value for the surface flux F_{q0}/w_* is close to what was obtained by eddy correlation, which was 0.06 g kg^{-1}. In contrast, the $z_* = 0.53$ curve intercepts the $z_* = 0.11$ curve at an unrealistically low value for sur-

face flux, and there is no intercept with the $z_* = 0.27$ curve.

To match the eddy correlation surface flux, the $z_* = 0.53$ curve would have to be lowered by about 20%. This could be accomplished by decreasing the variance by about 40%; however, such a decrease would be difficult to justify, considering that the variance during the three circles at $z_* = 0.53$ changes by considerably less than that: 0.126, 0.100, and 0.096 $(g/kg)^2$. An alternative approach would be to increase the top-down variance function f_t by about 40%. While *Moeng and Wyngaard*'s [1989] f_t plot shows some increase in f_t with decrease in grid size, it is highly unlikely that further decrease in grid size could increase f_t by as much as 40%. A more likely possibility is that cumulus convection (discussed in section 9) has increased the variances predominantly in the upper part of the CBL, so that the Moeng and Wyngaard variance functions no longer apply at the $z_* = 0.53$ level.

Another possible contributing factor is the stability condition across the top of the CBL under which the LES variance functions were obtained. Recent LES results by *Sorbjan* [1996] show that the shape of the humidity variance profile is sensitive to the potential temperature structure above the CBL. The sounding used for the *Moeng and Wyngaard* [1989] simulations had a virtual potential temperature increase across the inversion of 8 K, while for the case here, there is no discernible temperature jump across the CBL top, and a nearly wet adiabatic lapse rate above it. This is fairly typical of tropical marine CBLs. Thus, for flight 7, it would be desirable to use LES variance and gradient functions calculated for much less stable soundings than considered by Moeng and Wyngaard.

7.3. Species Lifetimes and Variance Estimates of Fluxes

The measured variances include not only contributions from actual atmospheric fluctuations of trace gas concentrations, but also contributions from errors in measurement. We can estimate the variance contribution from measurement errors by considering the measured variance for inert gases emitted into the atmosphere far from the measurement area and over an extended period of time. In that case, the variance is due solely to measurement errors. One of the trace gas species measured over 1 min intervals [*Blake et al.*, 1996] was an inert species, CFC-12, for which $\sigma_s/\langle S\rangle = 0.0086$.

Using the same approach that we used for the estimate of $(S_1 - S_2)/\langle S\rangle$ from the gradient technique (12), we again assume a steady state concentration, where the increase in a trace gas concentration from surface flux is balanced by chemical destruction, and negligible entrainment flux. The scalar budget equation (8) then becomes $F_{s0} = D_s/z_i$, so that (6) reduces to

$$\frac{\sigma_s}{\langle S\rangle} \approx \frac{\tau_t}{\tau_s} f_b^{0.5}. \tag{20}$$

At $z_* = 0.11$, $f_b^{0.5} = 2.7$, and if the variance from measurement errors for a nonconserved species is the same as for CFC-12, (20) gives a chemical lifetime of $\tau_s = 3.7$ days for the conditions of flight 7. That is, it would not be possible, in general, to estimate the surface emission flux using fluctuations generated directly by eddies that scale with z_i for a trace species with a lifetime longer than about 4 days for the conditions of this flight. This excludes, for example, $CHBr_3$, CH_3ONO_2, and $C_2H_5ONO_2$ (Table 1), and makes evaluation of the surface flux of CH_3I a borderline procedure.

On the other hand, the normalized standard deviations (given in parentheses) for $CHBr_3$ (0.054), CH_3ONO_2 (0.045), $C_2H_5ONO_2$ (0.047), and CH_3I (0.047) are much larger than for CFC-12, and the lifetimes calculated from these variances are considerably shorter than current theoretical estimates of their chemical lifetimes, which are 10–25 days for $CHBr_3$, CH_3ONO_2, and $C_2H_5ONO_2$, and 4 days for CH_3I (Table 1). In other words, the variances measured for these species on the mesoscale are much larger than the z_i-scaled variance predicted by mixed-layer similarity. The reason is that the mesoscale contributions to the variance involve processes that occur at much longer temporal and spatial scales than the variance due to emission from a horizontally homogeneous surface. Variability at these scales is generated by, for example, transport of CBL air into the BuL by sporadic events such as cumulus convection or Kelvin-Helmholtz instabilities across the CBL top. This is followed by differential horizontal advection and intermittent localized turbulence diffusion in the BuL, which has a much longer time scale than mixed-layer turbulence. That is, the redistribution process in the BuL is much slower than in the CBL, so that both horizontal and vertical variations can persist for much longer times than in the CBL.

Concentrations of these photochemically reactive trace species in the BuL decrease with time after they are injected into the BuL, and are not replenished as rapidly as in the CBL where the ocean-emitted gases are efficiently mixed throughout on a timescale of a few tens of minutes. Thus the concentration difference between the CBL and the BuL increases at a rate proportional to the reaction timescale. Finally, intermittent horizontally heterogeneous entrainment events (likely, for the most part, to be the same events that transport CBL air into the BuL) transport BuL air back into the CBL. As a result, variance is generated on the scale of these mesoscale events that is proportional to the difference in concentration between the CBL and the BuL.

8. Relationships Among Mesoscale Variance, Entrainment and Surface Flux

Here we consider a simple model to show how variance in the CBL is generated by mesoscale processes, which for reactive species emitted at the surface, can be related to surface flux. We consider a simple CBL of mean concentration $\langle S\rangle$ capped by a BuL of thickness h and mean concentration S_{Bu}. We assume both are in steady state, and define entrainment velocities w_{ea} entraining BuL air into the CBL and w_{eb} entraining CBL air into the BuL. For this analysis we assume diurnal averaging, so that the relevant chemical reaction rate is denoted by τ_s. Integrating the scalar budget equation (8) across the CBL, assuming horizontal homogeneity and negligible mean motion gives

$$\frac{F_{s0}}{z_i} + \frac{w_{ea}(S_{Bu} - \langle S\rangle)}{z_i} - \frac{\langle S\rangle}{\tau_s} = 0, \tag{21}$$

and integrating across the BuL gives

$$\frac{w_{eb}}{h}(\langle S\rangle - S_{Bu}) - \frac{S_{Bu}}{\tau_s} = 0. \tag{22}$$

Equation (22) can be solved for the jump across the CBL top $\Delta S = S_{Bu} - \langle S\rangle$,

$$\Delta S = -\langle S\rangle\left(\frac{1}{1 + \tau_s w_{eb}/h}\right). \tag{23}$$

This relation between the jump and the species lifetime provides a basis for the concentration differences assumed in obtaining (23).

We assume that the variance measured by the grab samples, which is obtained from an average over a 6 km collection distance, is generated solely by mesoscale variability; that is, that fluctuations in species concentration that are generated by surface emission are transported throughout the CBL by eddies that scale with z_i, and thus do not contribute significantly to variance at scales $\gg z_i$. In the case of entrainment, we consider two sources of fluctuations. One is fluctuations generated by turbulent eddies in the CBL resulting from shear and buoyancy flux. These eddies again scale with z_i and penetrate far enough into the capping inversion that they bring down air from the BuL into the CBL. This part of the entrainment flux still scales with z_i [e.g., *Moeng and Wyngaard* 1989]. The other part is generation of fluctuations by mesoscale processes such as cloud-related entrainment and horizontal variations in stability within the BuL and between the BuL and the CBL. The variance generated by these processes is at distinctly longer horizontal scales than that generated by turbulence that scales with the CBL depth. Furthermore, in contrast to the turbulent eddies generated by buoyancy and shear, these events can also transport CBL air into the BuL. However, we argue that the variance generated by these longer-scale processes should still obey the same scaling behavior as the z_i-scaled processes considered in (6), although likely with a different (larger-valued) variance function. The basis for this is that they generate concentration differences in the CBL in the same way as smaller-scale turbulence, but since the variance is at longer horizontal scales it will persist for longer time periods (and thus be mixed more thoroughly throughout the CBL before being dissipated) than at CBL scales.

Thus, from (6), the mesoscale standard deviation generated by flux due to entrainment on the mesoscale is

$$\tilde{\sigma}_s = \frac{\tilde{F}_{st}}{w_*}\varphi_t^{1/2}, \tag{24}$$

where φ_t is the top-down variance function (analogous to f_t for CBL-scale turbulence) applicable to these larger scales and $\tilde{F}_{st} = -\tilde{w}_{ea}\Delta S$ is the mesoscale entrainment flux. From (23) and (24) the normalized CBL standard deviation becomes

$$\frac{\tilde{\sigma}_s}{\langle S\rangle} = \frac{\tilde{w}_{ea}}{w_*}\left(\frac{1}{1 + \tau_s w_{eb}/h}\right)\varphi_t^{1/2}. \tag{25}$$

If we consider two reactive species, R and S, we can calculate the ratio of their normalized standard deviations using (25),

$$\frac{\tilde{\sigma}_r/\langle R\rangle}{\tilde{\sigma}_s/\langle S\rangle} = \frac{\tau_s + h/w_{eb}}{\tau_r + h/w_{eb}}. \tag{26}$$

Typical values of the variables are $h \sim 1000$ m and $w_{eb} \sim 10^{-2}$ m s^{-1}, so that $h/w_{eb} \sim 10^5$ s. Thus we can expect to see differences in the mesoscale variance generated by differences in reaction times of up to several days. Therefore, if we measure the normalized standard deviations of two species, know the lifetime of one species, and can estimate h/w_{eb}, we can estimate the lifetime of the other species. Alternatively, we can use (25) to solve for the ratio of the reaction time scales,

$$\frac{\tau_r}{\tau_s} = \frac{\varphi_t^{1/2}\dfrac{\tilde{w}_{ea}}{w_*}\left(\dfrac{\tilde{\sigma}_r}{\langle R\rangle}\right)^{-1} - 1}{\varphi_t^{1/2}\dfrac{\tilde{w}_{ea}}{w_*}\left(\dfrac{\tilde{\sigma}_s}{\langle S\rangle}\right)^{-1} - 1} \tag{27}$$

where both $\varphi_t^{1/2}\dfrac{\tilde{w}_{ea}}{w_*}\left(\dfrac{\tilde{\sigma}_r}{\langle R\rangle}\right)^{-1}$ and $\varphi_t^{1/2}\dfrac{\tilde{w}_{ea}}{w_*}\left(\dfrac{\tilde{\sigma}_s}{\langle S\rangle}\right)^{-1} > 1$. In this form, however, we need to know w_*, $\tilde{w}_{ea}$, and the variance function φ_t. This is, in some sense, analogous to the arguments used by, for example, *Colman et al.* [1998] to estimate atmospheric residence times of the order of a year for nonconserved species using species variability measured throughout the troposphere on intercontinental scales.

Similarly, from (21) and (24), if the species lifetime is known, the species surface flux can be estimated as

$$F_{s0} = \frac{z_i}{\tau_s}\langle S\rangle + w_*\tilde{\sigma}_s\varphi_t^{-1/2}. \tag{28}$$

Therefore, from (28), the ratio of surface fluxes for two species is

$$\frac{F_{r0}}{F_{s0}} = \left(\frac{\langle R\rangle\tau_s}{\langle S\rangle\tau_r}\right)\left(\frac{1 + w_* z_i^{-1}\varphi_t^{-1/2}\tau_r\tilde{\sigma}_r/\langle R\rangle}{1 + w_* z_i^{-1}\varphi_t^{-1/2}\tau_s\tilde{\sigma}_s/\langle S\rangle}\right). \quad (29)$$

A typical value for the factor multiplying the product of the reaction time and the normalized standard deviation is $w_* z_i^{-1}\varphi_t^{-1/2} \sim 10^{-3}$ s^{-1}. Furthermore, $\tilde{\sigma}_s/\langle S\rangle \sim 0.05$, so that for reaction times greater than about a day,

$$\frac{F_{r0}}{F_{s0}} \simeq \frac{\tau_s\tilde{\sigma}_r}{\tau_r\tilde{\sigma}_s}. \quad (30)$$

Table 1 shows normalized standard deviations for several species measured via the 1-min sample collection. Before computing the standard deviations, a linear trend in time was removed. Variances were computed for each circle within the CBL, which consisted of 5 or 6 samples per circle. The standard deviations in Table 1 were obtained from variances averaged over all circles. The results indicate that there is little variation in standard deviation from one species to another despite the estimated factor of six difference in species lifetimes indicated in Table 1. This could be due to either all the species lifetimes $\ll h/w_{eb}$ or that the actual species lifetimes are similar (i.e., the actual lifetimes differ from the theoretical estimates). The measured standard deviation for CFC-12, which is essentially a conserved species, is about a factor of 5 smaller than for the reactive species, which indicates that the accuracy of the measured differences is sufficient to resolve real fluctuations in the reactive species listed in Table 1.

9. Sources of Mesoscale Variability

The large-scale variations in humidity can, in part, be attributed to drift in the Lyman-alpha humidity probe. However, similar large-scale variations can also be seen in the more steady, slow-rate (1 s) specific humidity data derived from dew point temperature.

Figure 9 shows 1 s values of specific humidity, potential temperature, and sea surface temperature during the first and last circle at $z_* = 0.53$. We see variations in humidity on scales $10z_i$ to $100z_i$ (1 to 10 min). The humidity variations cannot be attributed to variations in sea surface temperature because it changes much more gradually. The variations in potential temperature and humidity tend to be inversely correlated. Since the sea surface was warmer than the overlying air, this suggests horizontal variability in the entrainment flux. This has been observed previously in a marine CBL (Q. Wang, et al., Characteristics of the marine boundary layers during two Lagrangian measurement

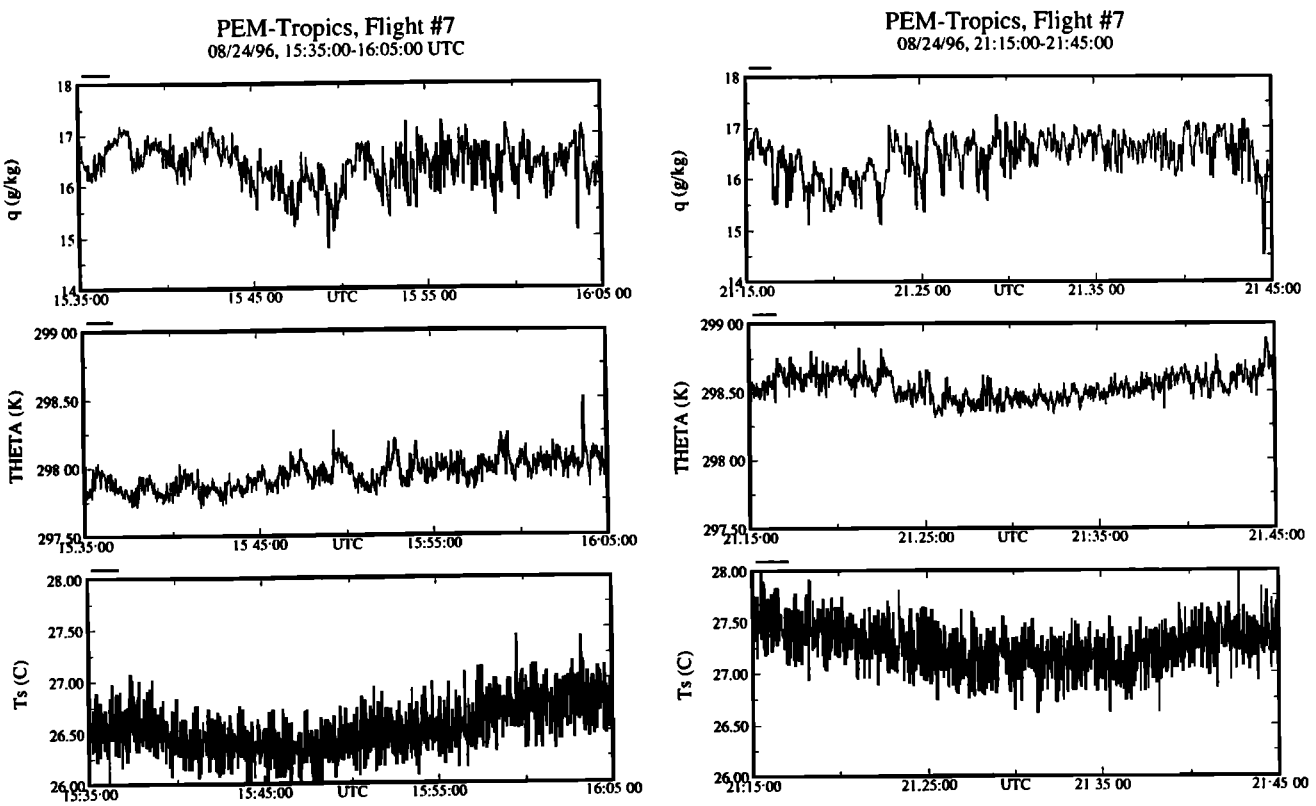

Figure 9. Variations in specific humidity (q), potential temperature (THETA), and surface temperature (Ts). These are 1 s data, collected 5.7 hours apart at $z_* = 0.53$. One minute = 6 km $\approx 10z_i$.

periods, 2, Turbulence structures, submitted to *Journal of Geophysical Research,* 1998, hereinafter referred to as Wang et al., submitted manuscript, 1998). Furthermore, we note that over the 5.7 hour time between the two circles, both the potential temperature and the sea surface temperature have increased by about 0.7 °C, but the specific humidity remains nearly the same, which suggests a near balance between the humidity gained due to evaporation from the sea surface and lost due to entrainment.

9.1. Cumulus Convection

A few small clouds above the CBL were noted by observers on the aircraft, and they are evident as dips in the ultraviolet (UV) radiation recorded by the upward pointing radiometer while the aircraft was circling in the CBL (Figure 10). To see if these clouds were advected, inactive cloud patches or small cumulus clouds (Cu) rising from the CBL, we look at humidity fluxes during the various constant altitude circles and semicircles within and above the CBL (Figure 11). To avoid mesoscale variations, the fluxes here represent wavelength $<5.3z_i$. For circles at $z_* < 1$ the fluxes are measured over the entire circle; for $z_* > 1$ the airplane alternated between two levels, with 5 min at each level around the circle so that the total sampling period is less than half the 30 min period available for circles $z_* < 1$.

The humidity fluxes for circles nearest the surface ($z_* = 0.11$) remain essentially constant during all three circles over a 6 hour period; at $z_* = 0.27$ and 0.53 they increase somewhat over time, but there are no well-defined changes with altitude indicative of significant flux convergence/divergence within the CBL. This is consistent with the nearly constant humidity in the CBL observed during the experiment (Figure 9). In contrast, above the boundary layer top, at $z_* = 1.1$, 1.33, and 1.6, the humidity fluxes are highly variable among runs at the same level, and the up and downward pointing UV radiometers indicate that the highest positive and negative fluxes are in regions with the most clouds.

Figure 12 shows data from a flight segment passing through a cloud at $z_* = 1.1$, where the upward pointing radiometer (UVZ) records a drop in UV radiation from above, while the downward pointing radiometer (UVN) shows an increase in UV radiation from below. Increases in radiation from below but with no changes in radiation from above, indicate that there are smaller clouds below the flight level. The expanded portion of the cloud penetration in Figure 12 shows that the high humidity regions associated with the cloud are, for the most part, in negatively buoyant downdrafts, which suggests that we are observing the dissipating stages of a small Cu.

The last plot in Figure 12 shows the potential temperature profile from a nearby aircraft sounding. Since this is a slantwise sounding, the small oscillations in potential temperature are likely due to horizontal variations. While the CBL is well-mixed, it is not capped by an inversion. Instead, it is topped by a BuL [*Russell et al.*, 1998] or cloud layer [e.g., *LeMone*, 1980], which here has a nearly wet-adiabatic lapse rate. Since there is no discernible temperature jump at the CBL top, large eddies carrying warmer, moister portions of the CBL air may easily rise into the BuL thus forming Cu clouds.

The UV radiometer data show that the small Cu are not randomly distributed, but appear in clusters with stretches of clear air in between (Figure 10). Over time, this type of nonuniform convection and the associated entrainment through the CBL top could produce mesoscale variations not only in the CBL humidity, but also in trace gases. Since the extent of these variations depends on the concentration differences across the CBL top, the resulting power spectrum for fluctuations in trace gas concentrations need not have the same shape as the power spectrum for humidity fluctuations.

9.2. Roll Organization

Horizontal roll vortices along the wind direction are often observed in CBLs [e.g., *Etling and Brown*, 1993]. To see if roll organization exists in this CBL, we examine cross-wind and along-wind portions of the constant altitude circles.

Figure 13 shows the vertical velocity power spectra in nearly cross-wind and nearly along-wind portions of the circle, at z_*= 0.53. The spectral peak is well defined in the cross-wind segments, whereas in the segments along the wind direction the peak spreads over a wide range of scales. The total variance is lower in the along-wind segments than in the cross-wind segments.

The time series of vertical velocity traces shown on the bottom of Figure 13 correspond to the power spectra directly above them. In the cross-wind segments the spacing between updrafts is somewhat variable, usually around $2z_i$ or $3z_i$, which is compatible with roll organization (z_i = 570 m, and each 10 s subdivision corresponds to about 1 km). The vertical velocities from the flight segment nearly along the wind direction suggest the presence of turbulent rolls intercepted at a wide angle.

Similar power spectra from cross-wind and along-wind portions of the flight are seen in data from other circles, but not consistently in every cross- or along-wind portion of the circle, which indicates that the roll organization is intermittent. While over a circular path the effects of roll organization tend to average out, intermittent roll organization could introduce some uncertainty in our scaling factor for relating the long and the short wavelength ends of the power spectrum.

9.3. Mesoscale Variations in the Horizontal Wind: How Well Did We Track the Air Mass?

Figure 14 shows TAMMS high-rate east and north wind components during two clockwise circles, 5 hours

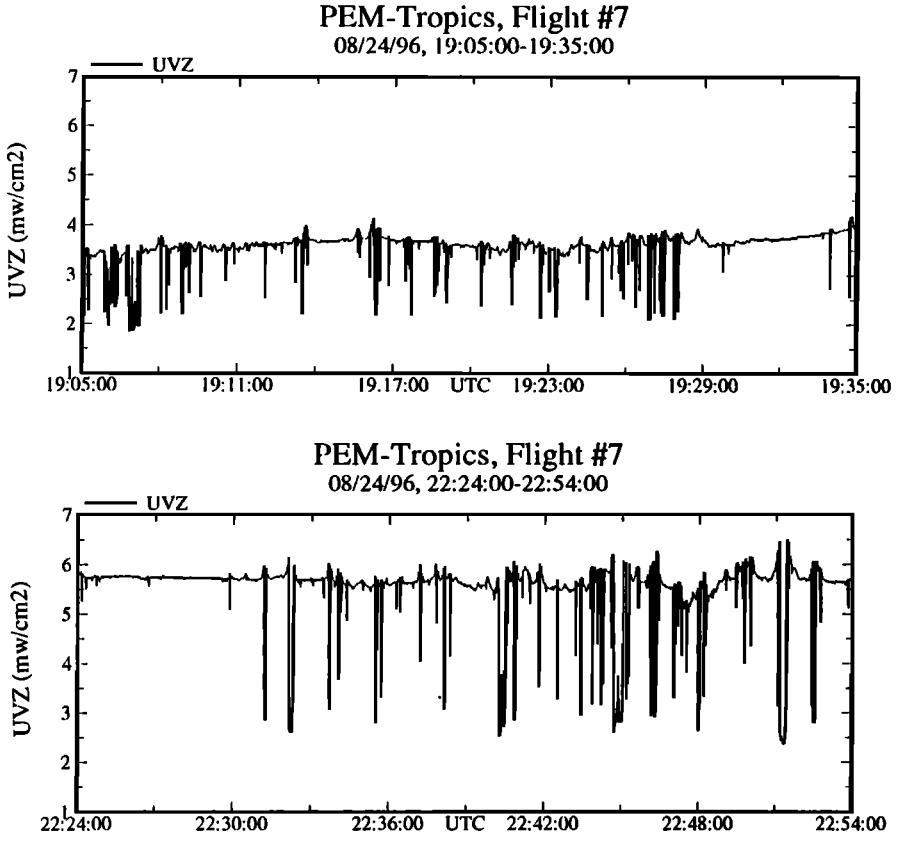

Figure 10. Distribution of clouds above the boundary layer as inferred from dips in UV radiation measured by the upward pointing radiometer. These data are from two clockwise circles in the boundary layer at 0905–0935 and 1224–1254 local time.

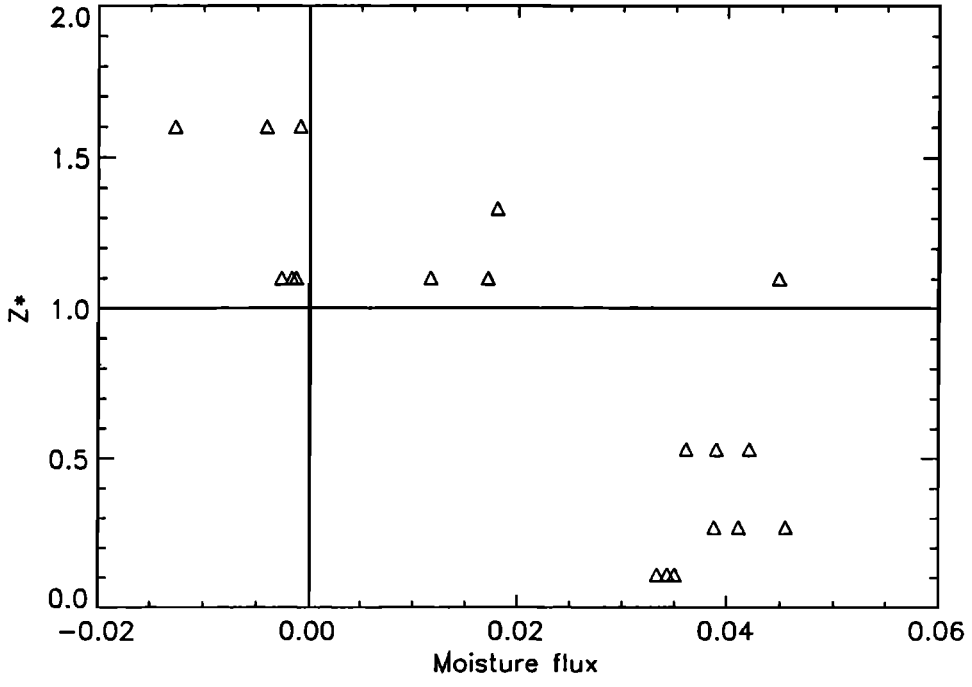

Figure 11. Humidity flux from wavelengths $<5.3z_i$ measured within and above the boundary layer. The highest fluxes above the boundary layer are associated with large patches of clouds.

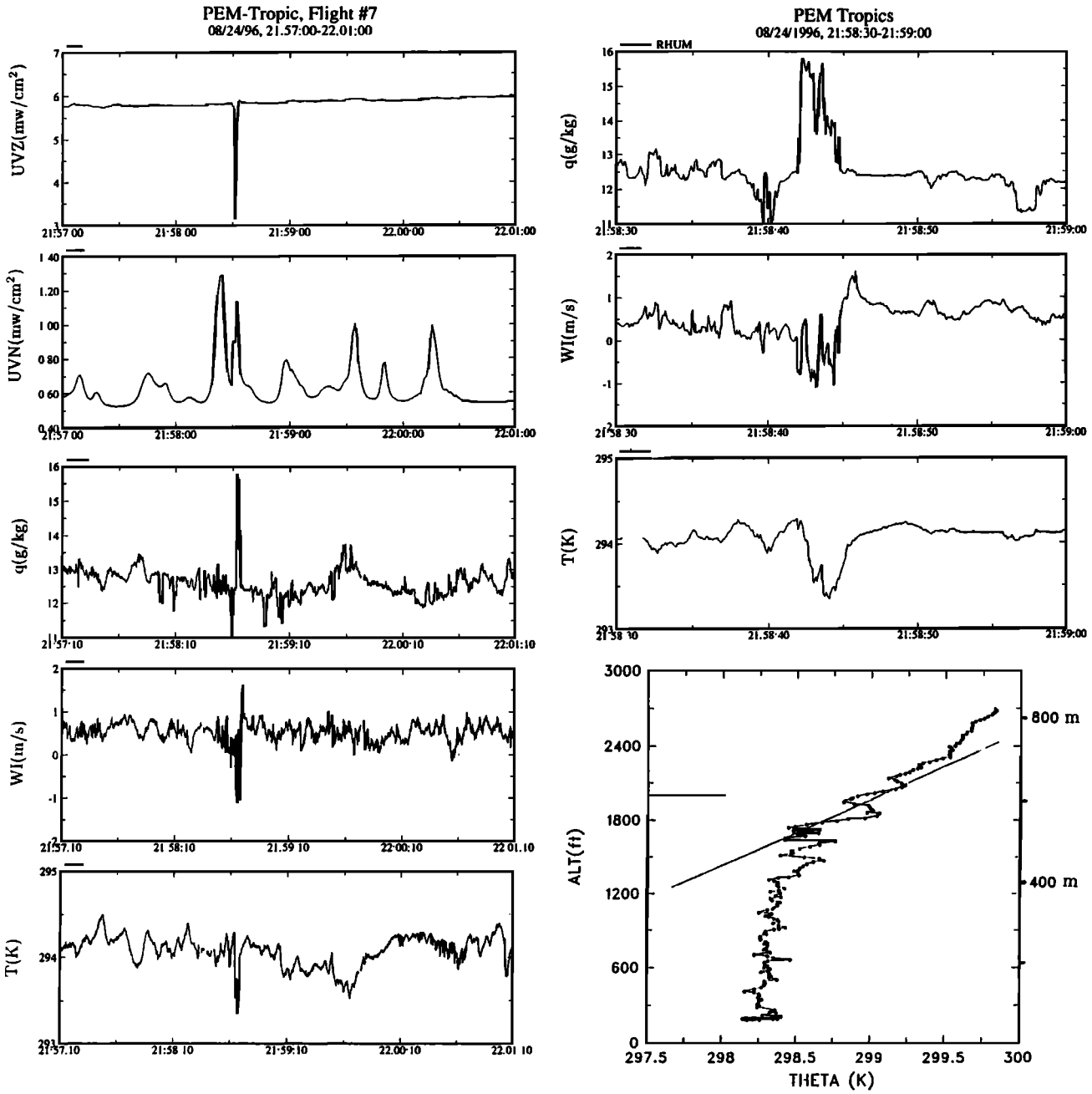

Figure 12. Evidence of cumulus convection: upward and downward UV radiation (UVZ and UVN) with 1 s resolution, and high-rate data of specific humidity (q), vertical velocity (WI), and temperature (T) during a 3 min (18 km) flight segment at $z_* = 1.1$. A 10 s time adjustment between the slow- and high-rate data has been incorporated. An expanded portion of the flight segment from the neighborhood of the cloud is shown to the right. The plot on the lower right shows the potential temperature (THETA) profile; the sloping line shows the wet-adiabatic lapse rate, and the horizontal line marks the flight altitude for the time series plots.

40 min apart, at $z_* = 0.27$. Here and in other constant altitude circles (not shown), the wind at the northern end of the circle is persistently 2-3 m s^{-1} stronger than at the southern end, and there are variations on smaller scales as well. These variations can be expected to introduce variability in the air trajectories along the flight track, and thus the observed mesoscale variations may, in part, reflect different past histories of the air sampled.

The positions of the circles were adjusted to follow the air mass trajectory using the Flight Management System wind velocity, which has a relatively slow response time. The TAMMS high-rate velocities, processed after the flight, are expected to be more accurate. The lower plot in Figure 14 shows the flight tracks (solid lines) during the two circles. The dashed line shows the approximate position of the first circle 5 hours 40 min later, assuming it is traveling with the wind observed during the first circle. The circle has been stretched,

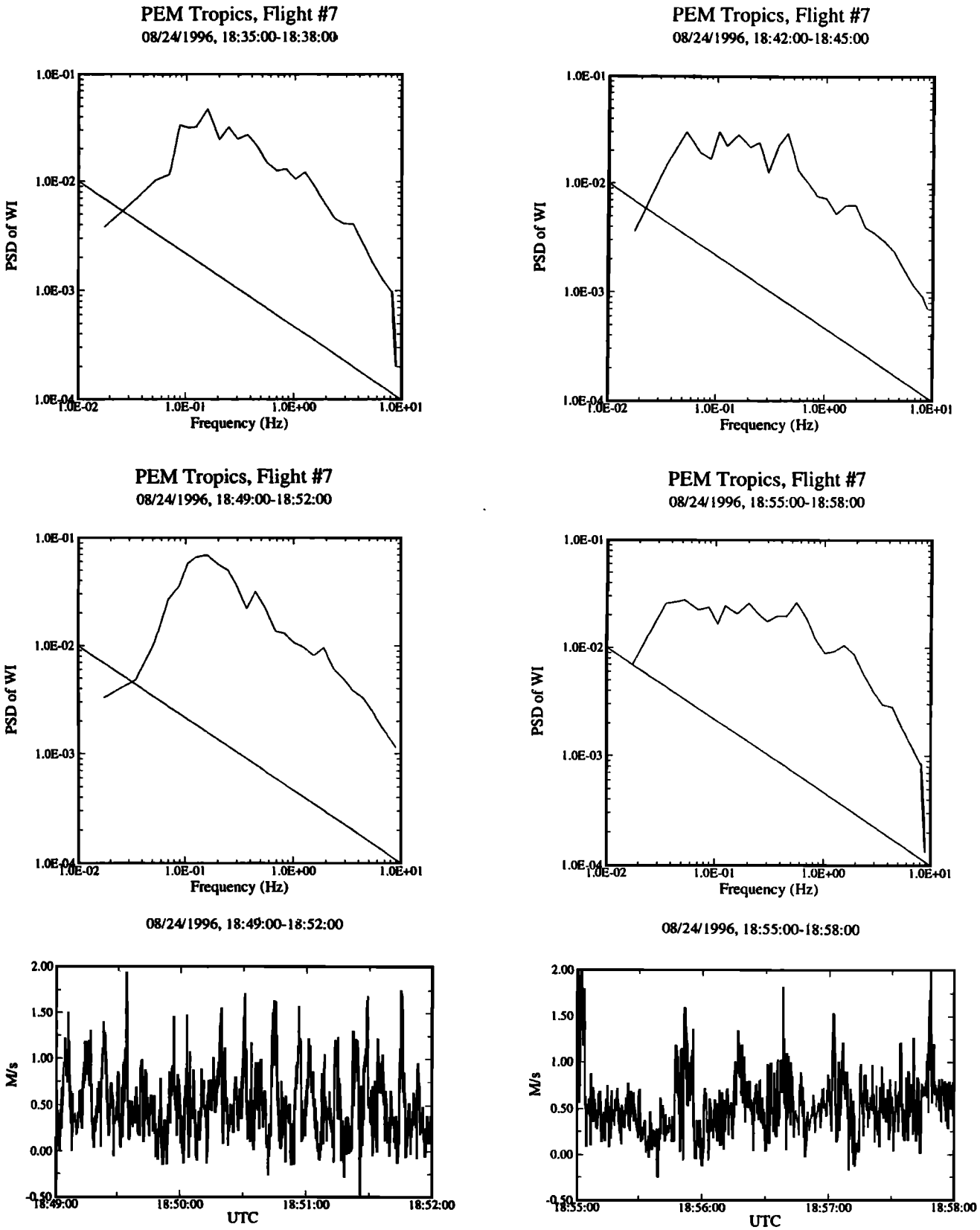

Figure 13. Some evidence of roll organization: vertical velocity power spectra from the (left) cross-wind and (right) nearly along-wind flight directions for 3 min (18 km) flight segments during circles at $z_* = 0.53$. Below are time series of vertical velocity traces for the power spectra directly above. The diagonal line in the power spectra plots shows the 2/3 slope, characteristic of turbulence in the inertial subrange.

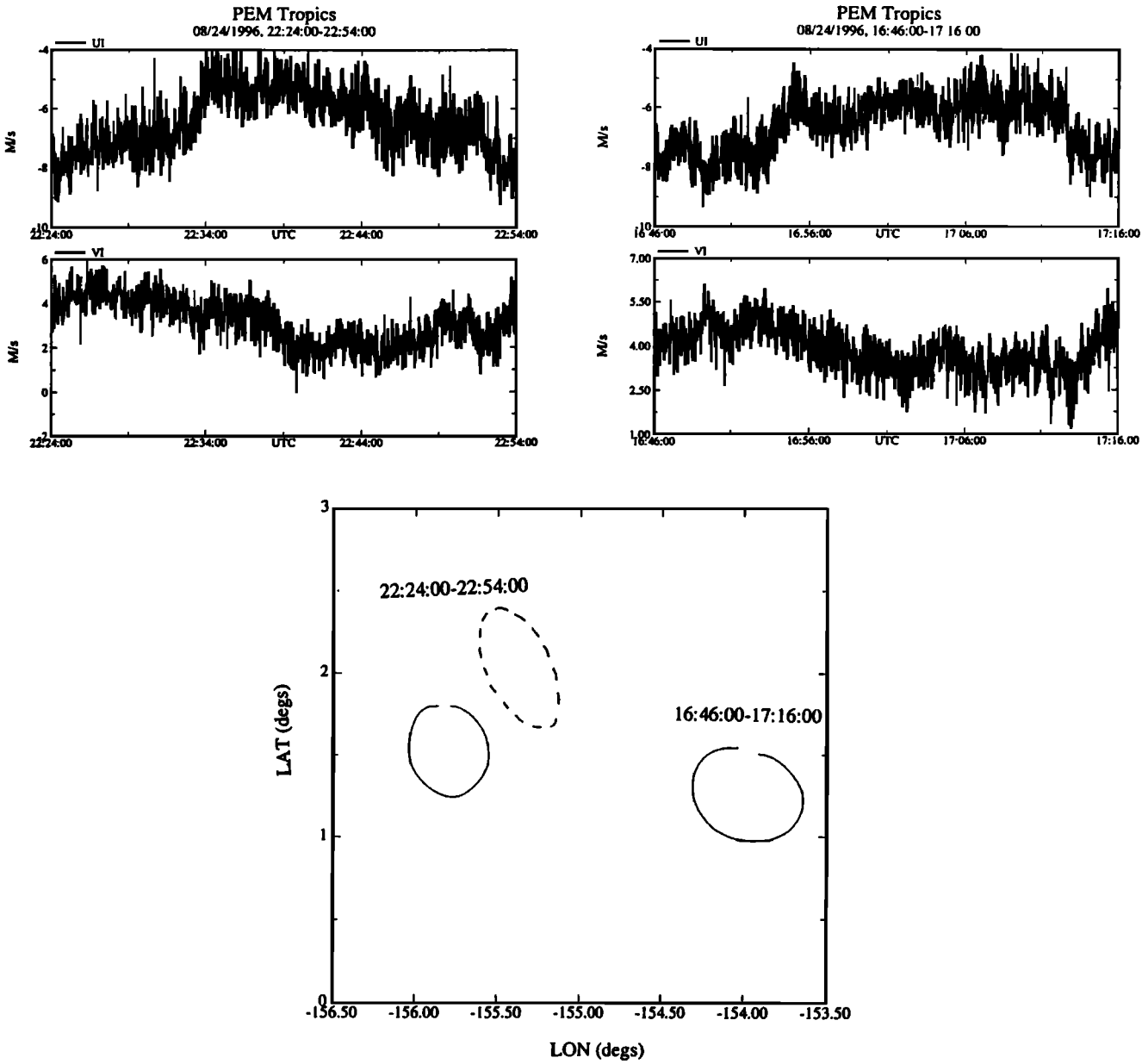

Figure 14. Variations in the east and north wind components (UI and VI) during two clockwise circles, 5 hours 40 min apart, at $z_* = 0.27$. Below is the flight track (solid lines). The dashed line shows the approximate position of the earlier circle 5 hours 40 min later assuming it is advected with the wind observed during the earlier circle. One degree $\approx$ 100 km.

and it is about 70 km NE of the actual 2224:00-2254:00 UT flight track.

The above illustrates the difficulties of following an air mass in the presence of variable and/or inaccurately measured horizontal wind. A ± 1 m s^{-1} error in the mean wind velocity will produce a ± 22 km error in position 6 hours later.

10. Optimal Flux Measurement Strategies

In this section we outline the procedures necessary to optimize measurement strategies in order to estimate surface fluxes of trace species by both the mixed-layer gradient and the variance techniques.

10.1. Using the Gradient Technique

As pointed out earlier, the accuracy of flux measurement by the gradient technique improves considerably as the height of the lowest measurement decreases because the concentration gradient increases. *Moeng and Wyngaard* [1984, 1989] found that the gradient changes approximately as $z_*^{-3/2}$ near the surface.) Thus, to optimize the accuracy of the flux measurement, the lowest flight level should be flown as low as possible. An added advantage is the concomitant decrease in

the integral scale of the turbulence as the height decreases [*Lenschow*, 1995], which means that the averaging length required for a specified measurement accuracy also decreases. On the other hand, LES does not necessarily accurately simulate flow in the lowest part of the CBL (the surface layer) because of the size of the grid used in the simulations, and deficiencies in the subgrid scale closure scheme. In fact, however, extrapolation of the LES results into the surface layer agrees well with measurements of both gradients and variances in the surface layer. Finally, since the gradient becomes small in the middle of the CBL, there is no need to obtain measurements at more than one level there. *Davis* [1992] has examined in detail various strategies for minimizing flux measurement errors using the gradient technique.

Another consideration for applying the gradient technique is the necessity for accurate measurements of height above the surface, especially close to the surface where the gradient becomes large. For example, a 20 m error in height translates roughly to a 20% error in the surface flux estimate for $z_* \simeq 0.1$ and $z_i \simeq 1000$ m. This points to the necessity of accurate geometric altitude measurements by, for example, a radio altimeter, rather than by correcting pressure altitude measurements.

Finally, for gases which are destroyed by photochemical reactions, it would be preferable to measure before sunrise or after sunset to avoid corrections for diurnal changes. Scattered clouds may also reduce the measurement accuracy both by introducing horizontal variability into the photochemical destruction rate and into the entrainment rate at the top of the CBL.

10.2. Using the Variance Technique

Here we distinguish between variance that scales with z_i, and mesoscale variance. For the z_i-scaled variance technique it is also important to select a horizontally uniform CBL, with minimal cloudiness, although the effects of mesoscale variability can, to some extent be mitigated by high-pass filtering. Again, as with the gradient technique, flying lower increases the measurement accuracy, but the rate of improvement is less than for the gradient technique. This also means that the variance technique is less sensitive to errors in altitude measurement.

To estimate z_i-scaled variance from grab samples, it is desirable to minimize the sampling time, so as to include as large a portion of the data from the shorter-wavelength end of the variance spectrum as possible. If the sampling time were reduced to 10 s, which is probably the shortest feasible collection time for flask samples, then the sampled variance would include wavelengths as small as 1 km, which is well within the regime where variance is generated in a horizontally homogeneous CBL by the surface fluxes rather than by mesoscale processes. The larger the number of samples, the better the accuracy. Presently, practical considerations probably limit the number of samples to about 140 per flight. If the samples are independent, the measured variance samples follow a chi-squared distribution. Therefore, if 10 samples are collected, there is a 90% probability that the measured standard deviation (which is proportional to the flux) will lie between the limits $0.6\sigma_{\hat{s}} < \sigma_s < 1.4\sigma_{\hat{s}}$, where $\sigma_{\hat{s}}$ is the actual standard deviation. For 41 samples the limits are $0.8\sigma_{\hat{s}} < \sigma_s < 1.2\sigma_{\hat{s}}$.

Fast-response measurements of a reference reactive scalar emitted from the surface would be very useful, in addition to humidity, for estimating a scaling factor to be applied to the grab-sampled variance estimates. DMS has ideal properties for this: a 1–2 day lifetime, a reasonably uniform surface source, and negligible solubility in cloud. A prototype chemiluminescence fast-response DMS sensor has been demonstrated in the laboratory by *Hills et al.* [1998].

For estimating mesoscale variance from grab samples, collection times of 1 min or more are appropriate. Although this technique, applied to a single species, would be difficult to implement in order to give quantitative estimates of lifetimes or surface fluxes, it may be possible to estimate lifetimes or surface fluxes for a target species by taking ratios of standard deviations of the target species with a species whose lifetime or surface flux is known. The advantages of the mesoscale variance technique is that it can be used with measurements obtained over averaging times of a minute or more, and it can be applied to species emitted from the ocean with lifetimes of perhaps a week or more.

11. Summary and Conclusions

Flight 7 during PEM-Tropics provided a good opportunity to observe diurnal changes within a Lagrangian framework. We have estimated the daytime destruction (production) rates under nearly clear skies for DMS, SO_2, $CHBr_3$, and CH_3I (Table 2). On this flight the DMS destruction and the SO_2 production rates balance each other. Using the mixed–layer gradient technique adjusted for diurnal variations, we estimate a DMS surface flux of 2.5 ± 1.0 pptv m s^{-1} ($6.1\pm2.4 \times 10^{13}$ molecules m^{-2} s^{-1}, or 8.8±3.4 μmols m^{-2} d^{-1}). The DMS flux is on the high side, but not incompatible with previous measurements.

We show that the gradient technique requires high measurement accuracy even with fairly short-lived trace gases. To estimate fluxes of the more long-lived trace gases that did not show surface gradients outside the expected errors, we attempted to use the mixed-layer variance technique. This approach did not lead to useful results because of long sample collection distances (6 km) and mesoscale variability. We show that the mixed-layer variance technique could be applied to relatively short-lived trace gases in cumulus-free CBLs that are horizontally more uniform, if shorter sampling times were used (of the order of 10 s or less). For tropical

marine CBLs it would be desirable to recompute the LES mixed-layer variance and gradient functions using soundings where the temperature jumps across the CBL top are weak to better simulate that regime.

The presence of species emitted from the ocean that have a lifetime of a few days or less above the CBL indicates that transport of CBL air into the overlying BuL occurs. This transport arises, for example, from clusters of small cumulus clouds rising into the BuL, or episodic shear-induced turbulence. These processes induce horizontal variations in entrainment flux and concentration on the mesoscale in both the CBL and the BuL. The timescale for these processes is longer than for turbulent fluctuations directly generated by surface fluxes. We show how this process can be used to estimate surface fluxes and lifetimes for species with lifetimes that are too long to estimate fluxes by mixed-layer gradients or variance directly associated with surface fluxes.

Acknowledgments. This research has been supported by NASA Langley Research Center order L-63196D. We thank Steve Oncley and Larry Mahrt, as well as the anonymous reviewers, for their comments. The National Center for Atmospheric Research is sponsored by the National Science Foundation.

References

Andreae, M.O., and T.W. Andreae, Cycle of biogenic sulfur compounds over the amazon basin, 1, Dry season, *J. Geophys. Res., 93*, 1487–1497, 1988.

Bandy, A.R., D.C. Thornton, R.G. Ridgeway Jr., and B.W. Blomquist, Key sulfur-containing compounds in the atmosphere and ocean: Determination by gas chromatography-mass spectrometry and isotopically labeled internal standards, in *Isotope Effects Gas-Phase Chemistry, ACS Symp. Ser., Vol. 502*, pp. 409–422, Am. Chem. Soc., Washington, D.C., 1992.

Bandy, A.R., D.C. Thornton, and A.R. Driedger III, Airborne measurements of sulfur dioxide, dimethylsulfide, carbon disulfide and carbonyl sulfide by isotope dilution gas chromatography/mass spectrometry, *J. Geophys. Res., 98*, 23,423–23,434, 1993.

Bandy, A.R., D.C. Thornton, B.W. Blomquist, S. Chen, T.P. Wade, J.C. Ianni, G.M. Mitchell, and W. Nadler, Chemistry of dimethylsulfide in the equatorial Pacific atmosphere, *Geophys. Res. Lett., 23*, 741–744, 1996.

Bates, T.S., J.E. Johnson, P.K. Quinn, P.D. Goldan, W.C. Kuster, D.C. Covert, and C.J. Hahn, The biogeochemical sulfur cycle in the marine boundary layer over the northeast Pacific Ocean, *J. Atmos. Chem, 10*, 59–81, 1990.

Bates, T.S., B.K. Lamb, A. Guenther, J. Dignon, and R.E. Stoiber, Sulfur emissions to the atmosphere from natural sources, *J. Atmos. Chem., 14*, 315–337, 1992.

Bates, T.S., K.C. Kelly, and J.E. Johnson, Concentrations and fluxes of disolved biogenic gases (DMS, CH_4, CO, CO_2) in equatorial Pacific during the SAGA 3 experiment, *J. Geophys. Res., 98*, 16,969–16,977, 1993.

Berresheim, H., F.L. Eisele, D.J. Tanner, L.M. McInnes, D.C. Ramsey-Bell, and D.S. Covert, Atmospheric sulfur chemistry and cloud condensation nuclei (CCN) concentrations over the northeastern Pacific coast, *J. Geophys. Res., , 98*, 12,701–12,711, 1993.

Blake, D.R., T.-Y. Chen, T.W. Smith Jr., C.J.-L. Wang, O.W. Wingenter, N.J. Blake, F.S. Rowland, and E.W. Mayer, Three-dimensional distribution of nonmethane hydrocarbons and halocarbons over the northwestern Pacific during the 1991 Pacific Exploratory Mission (PEM-West A), *J. Geophys. Res., 101*, 4377–4392, 1996.

Blomquist, B.W., A.R. Bandy, and D.C. Thornton, Sulfur gas measurements in the eastern North Atlantic Ocean during the Atlantic Stratocumulus Transition Experiment/Marine Aerosol and Gas Exchange, *J. Geophys. Res., 101*, 4377–4392, 1996.

Charlson, R.J., J.E. Lovelock, M.O. Andreae, and S.G. Warren, Oceanic phytoplankton, atmospheric sulphur, cloud albedo and climate: A geophysiological feedback, *Nature, 326*, 655–661, 1987.

Colman, J.J., D.R. Blake, and F.S. Rowland, Atmospheric residence time of CH_3Br estimated from the Junge spatial variability relation. *Science, 28*, 392–396, 1998.

Considine, J., B. Anderson, J. Barrick, and D.H. Lenschow, Characterization of turbulent transport in the marine boundary layer during flight 7 of PEM-Tropics A, *J. Geophys. Res.*, this issue.

Davis, D., et al., DMS oxidation in the equatorial Pacific: Comparison of model simulations with field observations for DMS, SO_2, H_2SO_4(g), MSA(g), and NSS, *J. Geophys. Res.*, this issue.

Davis, K.J., Surface fluxes of trace gases derived from convectivelayer profiles, Ph.D. dissertation, 281 pp., Univ. of Colo., Boulder, 1992. (Available as *NCAR/CT-139* from Natl. Cent. for Atmos. Res., Boulder, Colo.)

Davis, K.J., D.H. Lenschow, and P.R. Zimmerman, Biogenic nonmethane hydrocarbon emissions estimated from tethered balloon observations, *J. Geophys. Res., 99*, 25,587–25,598, 1994.

Eisele, F.L., and H. Berresheim, High-pressure chemical ionization flow reactor for real-time mass spectrometric detection of sulfur gases and unsaturated hydrocarbons in air, *Anal. Chem., 64*, 283–288, 1992.

Etling, D., and R. A. Brown, Roll vortices in the planetary boundary layer: A review, *Boundary-Layer Meteorol., 65*, 215–248, 1993.

Fuelberg, H.E., R.E. Newell, S. Longmore, Y. Zhu, D.J. Westberg, E.V. Browell, D.R. Blake, G.R. Gregory, and G.W. Sachse, A meteorological overview of the PEM-Tropics period, *J. Geophys. Res.*, this issue.

Hills, A.J., D.H. Lenschow, and J.W. Birks, Fast dimethyl sulfide measurement by flourine-induced chemiluminescence, *Anal. Chem., 70*, 1735–1742, 1998.

LeMone, M.A., The marine boundary layer, in *Workshop on the Planetary Boundary Layer*, edited by J.C. Wyngaard, 322 pp., Am. Meteorol. Soc., Boston, Mass., 1980.

Lenschow, D.H., Micrometeorological techniques for measuring biosphere-atmosphere trace gas exchange, in *Biogenic Trace Gases: Measuring Emissions From Soil and Water*, edited by P.A. Matson and R.C. Harriss, chap. 5, pp. 126–163, Blackwell Sci., Cambridge, Mass, 1995.

Lenschow, D.H., A proposal for measuring entrainment into the cloud-capped boundary layer, in *Proceedings of the ETL/CSU Cloud-Related Process Modeling and Measurement Workshop, Boulder, Colorado, 23-25 October 1995*, edited by A.S. Frisch, D.A. Randall, and W.H. Schubert, *NOAA ETL Rep.* 29–55, Natl. Oceanic and Atmos. Admin., Boulder, Colo., 1996.

Lenschow, D.H., J.C. Wyngaard, and W.T. Pennell, Mean-field and second-moment budgets in a baroclinic, convective boundary layer, *J. Atmos. Sci., 37*, 1313–1326, 1980.

Mann, J., and D.H. Lenschow, Errors in airborne flux measurement, *J. Geophys. Res., 99*, 14,519–14,526, 1994.

Moeng, C.-H., and J.C. Wyngaard, Statistics of conservative scalars in the convective boundary layer, *J. Atmos. Sci., 41*, 3161–3169, 1984.

Moeng, C.-H., and J.C. Wyngaard, Evaluation of turbulent transport and dissipation closures in second-order modeling, *J. Atmos. Sci., 46*, 2311–2330, 1989.

Russell, L.M., D.H. Lenschow, K.K. Laursen, P.B. Krummel, S.T. Siems, A.R. Bandy, D.C. Thornton, and T.S. Bates, Bidirectional mixing in an ACE 1 marine boundary layer overlain by a second turbulent layer, *J. Geophys. Res., 103*, 16,411–16,432, 1998.

Sorbjan, Z., Effects caused by varying the strength of the capping inversion based on large eddy simulation model of the shear-free convective boundary layer, *J. Atmos. Sci., 53*, 2015–2024, 1996.

Wyngaard, J.C., and R.A. Brost, Top-down and bottom-up diffusion in the convective boundary layer, *J. Atmos. Sci., 41*, 102–112, 1984.

A.R. Bandy and D.C. Thornton, Department of Chemistry, Drexel University, Philadelphia, PA 19104.

D.R. Blake and I. Simpson, Department of Chemistry, Univesity of California, Irvine, CA 92717.

D.H. Lenschow and I. R. Paluch, National Center for Atmospheric Research, P.O. Box 3000, Boulder, CO 80307. (e-mail: lenschow@ucar.edu)

(Received July 27, 1998; revised November 25, 1998; accepted December 2, 1998.)